

2

DTIC

SECRET  
JUN 24 1991  
C

FTD-ID(RS)T-0811-90

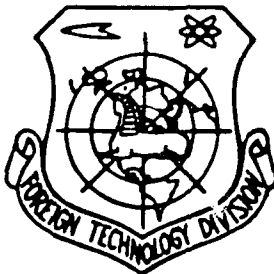
AD-A237 263



FOREIGN TECHNOLOGY DIVISION



CHINESE PHYSICS LASERS  
(Selected Articles)



Accession for	
DTIC GRA&I	<input checked="" type="checkbox"/>
DTIC TAB	<input type="checkbox"/>
Unannounced	<input type="checkbox"/>
Justification	
By	
Distribution/	
Availability Codes	
Avail and/or	
Dist	Special
A-1	

Approved for public release;  
Distribution unlimited.



91-02916



## HUMAN TRANSLATION

FTD-ID(RS)T-0811-90

11 April 1991

MICROFICHE NR: FTD-91-C-000290

CHINESE PHYSICS LASERS (Selected Articles)

English pages: 85

Source: Zhong Guo Jiguang, Vol. 16, Nr. 11,  
1989, pp. Title Page; 675-703

Country of origin: China

Translated by: Leo Kanner Associates  
F33657-88-D-2188

Requester: FTD/TTTD/Cason

Approved for public release; Distribution unlimited.

THIS TRANSLATION IS A RENDITION OF THE ORIGINAL FOREIGN TEXT WITHOUT ANY ANALYTICAL OR EDITORIAL COMMENT. STATEMENTS OR THEORIES ADVOCATED OR IMPLIED ARE THOSE OF THE SOURCE AND DO NOT NECESSARILY REFLECT THE POSITION OR OPINION OF THE FOREIGN TECHNOLOGY DIVISION

PREPARED BY:

TRANSLATION DIVISION  
FOREIGN TECHNOLOGY DIVISION  
WPAFB, OHIO

TABLE OF CONTENTS

Graphics Disclaimer .....	11
Successful Target Hit by China's First High-Power Double-Frequency Laser .....	1
Optical Bistability in Nematic Liquid Crystals, by Lin Zhemin, Chen Shuchao, Zhou Haiguang .....	3
Binocular Stereoscopic Holograms for Three-Dimensional Display, by Kang Hui, Yang Yingmin .....	17
Study of Phosphate Laser Glass with High Neodymium Concentration, by Mao Hanfen, Mao Sen, Li Jie, Jiang Yanyan, Jiang Yasi .....	29
Stress-Strain State of Slab Amplifiers, by Ding Liming, Yang Fumin, S.R. Bowman, J. Fogleman, C.O. Alley .....	35
Gain Saturation Parameters and Their Variation in Transverse-Flow Discharge CO <sub>2</sub> Lasers, by Wu Zhongxiang .....	44
Influence of Electrode Material on Operating Life of Line-Selection CO-CO <sub>2</sub> Compound Lasers, by Gui Zhenxing, Zhang Shunyi, Shen Guirong .....	51
Space-Variant Optical Logic Operation with $\theta$ -Modulation, by Chen Henguang, Lu Wenpei, Zhong An .....	57
XeCl-Laser-Induced Oxidation Reaction of Cerium Separation, by Zhou Zhenghuo, Qiu Mingxin, Huang Shaitang, Bu Qixiu, Gu Jialiang, Li Fangling, Shi Jiliang .....	65
Resonance Fluorescence Shift in Mg Atomic Isotopes with Ultraviolet Laser, by Wang Yuzhi, N. Beverini, F. Strumia .....	72
Ideal Size of Laser Spot in Laser Printing and its Measurement, by Li Qingxiong, Qian Qiuming, Zhao Jianming .....	77

GRAPHICS DISCLAIMER

All figures, graphics, tables, equations, etc. merged into this translation were extracted from the best quality copy available.

SUCCESSFUL TARGET HIT BY CHINA'S FIRST HIGH-POWER  
DOUBLE-FREQUENCY LASER

To direct experimental research on interaction between shortwave laser beam and matter, the authors conducted target hitting with a double-frequency laser with an LF-11\* laser device on 29 August 1989.

Emitted with an LF-11\* device, an intense collimated laser beam impinged on a KDP crystal with OD70mm; the laser beam was  $1.06\mu\text{m}$ , linear resonance and with OD64mm. The optimization system for the matching angle controlled with a microcomputer automatically adjusted the azimuth of the crystal for matching with the phase; an automatic temperature adjustment and control device was used to maintain constant temperature (temperature variation  $\leq 0.2^{\circ}\text{C}$ ) of the crystal. Television was used to control focusing; the positioning system made automatic adjustments on the micro-target. A streak camera, a calorimeter, a near-field camera and a far-field array camera were used to monitor the pulse duration, power density, light beam quality and other parameters of the fundamental frequency pump light and the output double-frequency light.

The typical frequencies achieved at the present time were as follows: when the fundamental frequency light power density was  $0.8\text{GW}/\text{cm}^2$  (energy 14.3J and pulse duration 580ps), the external conversion efficiency is greater than or equal to 62% for the

double-frequency energy; while passing through the OD100 $\mu$ m hole target, the energy transmissibility was  $\geq 93.6\%$ .

This high-power double-frequency laser has begun to be used in experimental research on inertially constrained fusion.

The paper was received on 27 December 1989; the authors are Wei Xiaofeng, Zhang Xiaomin, and Ye Jinxiang et al., Southwest Research Institute of Nuclear Physics and Chemistry.

## OPTICAL BISTABILITY IN NEMATIC LIQUID CRYSTALS

Lin Zhemin, Chen Shuchao and Zhou Haiguang, physics department,  
Xiamen University, Xiamen

Abstract: In this paper, the authors applied the gaussian light beam transmission matrix with the geometric-optics approximation analytical method; thus, the analytical results with a nematic liquid-crystal light self-focussing and optical bistability were obtained. Some experimental phenomena were recorded with EBBA (4-ethoxy-4'-n-butyl-benzyl-Lideneaniline) liquid crystal specimens. This once more proved that bistability is traceable to the photo-reorientation effect.

Key technical terms: EBBA, optical bistability.

The authors conducted an experimental determination of the liquid-crystal material EBBA. Within the temperature range (37 to 80°C) of the nematic phase of the material, the authors observed phenomena of self-focussing and feedback-type optical bistability. By using the analytical method of the geometric-optics transmission matrix for gaussian light beams, clarified theoretical models were derived, and brief analytical results were obtained, thus satisfactorily explaining some experimental phenomena.

### I. Theoretical Analysis

By utilizing the fundamental transverse mode polarized light beam ( $\text{Ar}^+$  514.5nm) as the input light, the direction of propagation was the Z-axis with the angle of incidence  $\phi_0$  and the polarized direction in the plane of the paper surface. The liquid crystal (EBBA) was oriented along the surface; the angle of orientation  $\hat{n}_0$  direction also lay within the plane of the paper surface (Fig. 1). Therefore, the angle of incidence appeared as the extraordinary ray. Based on the theory of continuum elastic bodies of nematic liquid crystals, with the approximation of the so-called single-elasticity coefficient, strong anchoring, and small reorientation angle, the field reorientation angle can be expressed as Eq. (1):

$$\theta(r, z) = \frac{(\Delta\epsilon)\sin 2\phi_0}{16\pi K} (d \cdot z - z^2) |E|^2 \quad (1)$$

In the equation,  $\Delta\epsilon \equiv \epsilon_{\parallel} - \epsilon_{\perp}$  indicates the anisotropy of the dielectric constant,  $K$  is the modulus of elasticity, and  $|E|^2$  is proportional to total light intensity.

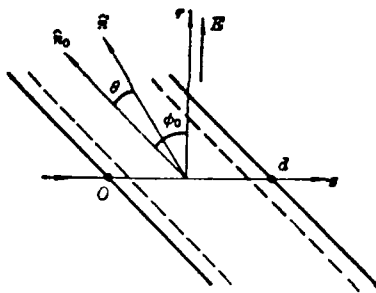


Fig. 1. Relationship between liquid-crystal arrangement and angle

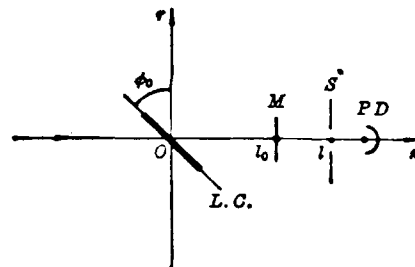


Fig. 2. Diagram of light path

The incident light was a fundamental transverse mode gaussian light beam. Fig. 2 shows an experimental light path. In the figure,  $M$  is the semilens (the index of reflection  $R$  is greater than 95%).  $S$  is a pinhole diaphragm.

The electric-field gaussian distribution of the incident light and the feedback light was expressed, respectively, as follows [2]:

$$\begin{cases} E_f(r, z) = E_{0f} \frac{W_{0f}}{W_f(z)} \cdot \exp - \left[ \frac{r^2}{W_f^2(z)} \right] \\ \times \exp \left\{ -i \left[ kz + \frac{kr^2}{2R_f(z)} \right] \right\} \end{cases} \quad (2a)$$

$$\begin{cases} E_b(r, z) = E_{0b} \frac{W_{0b}}{W_b(z)} \cdot \exp - \left[ \frac{r^2}{W_b^2(z)} \right] \\ \times \exp + i \left[ k(z - l_0) + \frac{kr^2}{2R_b(z)} \right] \end{cases} \quad (2b)$$

In the equations,  $W_0$  is the radius of the beam waist;  $W(z)$  is the radius of the light spot;  $R(z)$  is the radius of the wavefront curvature; the subscripts f and b indicate the positive and negative directions;  $l_0$  is the coordinate of the reflector length M.

The paper is confined to a discussion of the bistability phenomenon of integrated light intensity along the axis. If the diameter of the pinhole S is smaller than the size of the light spot in a gaussian light beam, but is much greater than the wavelength of the light, the diffraction effect of the aperture is not significant. In this case, a geometric-optics description can be adopted (see [3]).

By utilizing the theory of geometric-optical transmission matrix of a gaussian light beam [2] for analysis, let

$$A \equiv \frac{E_{0f} \cdot W_{0f}}{W_f(0)}, \quad B \equiv \frac{E_{0b} W_{0b}}{W_b(0)} \quad (3)$$

Obviously,  $|A|^2$  is determined by the forward-direction incident light intensity  $I_f(0)$  of the liquid crystal layer ( $z=0$ ). However, B is related to the feedback intensity of the feedback light beam in the liquid crystal layer. Different B values correspond to different integrated output light intensity  $I_f(l)$  after passing through the pinhole. As indicated by experiments, after adding a reflector M, the feedback-type optical bistability phenomenon appears; that is, for a certain input light intensity  $I_f(0)$ , there are two stability states of  $I_f(l)$  that separately correspond to the same value of  $I_f(0)$  at ascending and

descending. With removal of feedback, the phenomenon of optical bistability disappears; the value of  $I_f(1)$  corresponds to the value  $I_f(0)$ . However, a nonlinear relationship exists between the input and output light intensities.

From Eq. (2), the overall electric field in the liquid layer is

$$\begin{aligned}
 |E|^2 = |E_1 + E_2|^2 = & |A|^2 \exp\left[-\frac{2r^2}{W_1^2(0)}\right] \\
 & + |B|^2 \exp\left[-\frac{2r^2}{W_2^2(0)}\right] + 2A \\
 & \times B \exp -r^2 \left[ \frac{1}{W_1^2(0)} + \frac{1}{W_2^2(0)} \right] \} \\
 & \times \cos \left[ 2kz - kl_0 + \frac{kr^2}{2} \right. \\
 & \left. \times \left( \frac{1}{R_1(0)} + \frac{1}{R_2(0)} \right) \right]
 \end{aligned} \tag{4}$$

Considering that  $W(z)$  and  $R(z)$  are slowly-varying functions of  $z$ , within the range of the liquid-crystal layer ( $d$  at 50 to 100  $\mu\text{m}$  is much smaller than the confocal parameter  $\pi W_0^2/\lambda$  after the gaussian light beam). It can be considered that  $W$  and  $R$  are not related to  $z$ .

By utilizing the condition of  $r < W$ , let us expand the first two terms of Eq. (4):

$$\begin{aligned}
 \exp\left[-\frac{2r^2}{W_1^2(0)}\right] & \approx 1 - \frac{2r^2}{W_1^2(0)}, \\
 \exp\left[-\frac{2r^2}{W_2^2(0)}\right] & \approx 1 - \frac{2r^2}{W_2^2(0)}
 \end{aligned}$$

From Fig. 1, the included angle between the electric field  $\mathbf{E}$  (by neglecting the slight distinction in direction of  $\mathbf{E}$  and  $\mathbf{D}$ ) and the orientation vector  $\hat{n}$  is  $(\phi_0 - \theta)$ ; then the refractive index of the extraordinary ray is [8]

$$n_e(r, z) = \left[ \frac{\sin^2(\phi_0 - \theta)}{n_1^2} + \frac{\cos^2(\phi_0 - \theta)}{n_2^2} \right]^{-\frac{1}{2}} \tag{5}$$

When the above equation is developed with a small orientation angle  $\theta$ , then we obtain

$$\begin{cases} n_e(r, z) \simeq n_e(\phi_0) + b\theta(r, z) \\ n_e(\phi_0) = \left[ \frac{\sin^2 \phi_0}{n_e^2} + \frac{\cos^2 \phi_0}{n_o^2} \right]^{-\frac{1}{2}} \\ b = \frac{n_e n_o (n_e^2 - n_o^2) \sin 2\phi_0}{2[n_e^2 \sin^2 \phi_0 + n_o^2 \cos^2 \phi_0]^{\frac{3}{2}}} \end{cases} \quad (6)$$

Obviously,  $n_o(\phi_0)$  is the linear portion (with size between 1 and 2) of the refractive index of the extraordinary ray; however,  $b$  indicates the reorientation nonlinear effect of the refractive index.

Similarly, since the thickness  $d$  of the liquid crystal layer is much smaller than the radius  $r$  of the light spot, by utilizing the average refractive index  $\bar{n} \equiv \frac{1}{d} \int_0^d n(r, z) dz$  is used to replace the actual spatial distribution of the two-dimensional refractive index. The result was proved to be rational.

Noting that the third term at the right-hand side of Eq. (4) is the special periodic function. The special period  $\Lambda = \pi/k$  ( $k$  is the number of light waves) is much smaller than the thickness  $d$  of the liquid crystal, so the contribution made by the term to the average value of integration  $\bar{n}$  approaches zero. Obviously, the value of the phase shift of the reorientation effect caused by the optical-frequency electric field is determined by the first two terms on the right-side of Eq. (4).

From Eqs. (6), (1) and (4), we can obtain:

$$\left\{ \begin{array}{l} \bar{n}_e(r) = c_1 - c_2 r^2 \\ c_1 = n_e(\phi_0) \\ \quad + \frac{bd^2(\Delta\epsilon)\sin 2\phi_0}{96\pi K} (|A|^2 + |B|^2) \\ c_2 = \frac{bd^2(\Delta\epsilon)\sin 2\phi_0}{48\pi K} \\ \quad \times \left( \frac{|A|^2}{W_f^2(0)} + \frac{|B|^2}{W_g^2(0)} \right) \end{array} \right. \quad (7)$$

As indicated by Eq. (7), the liquid crystal layer is equivalent to a thin lens with distribution of refractive index squared. The pinhole diaphragm is placed at  $z=1$  (see Fig. 2) behind the reflector lens M. By using the light transmission matrix for a gaussian light beam, the parameters of the light beam at 1 can be determined. From the law of [ABCD] [2], we have

$$q_1 = \frac{Aq_0 + B}{Cq_0 + D} \quad (8)$$

In the equation,  $q_0$  indicates the parameter of the input light beam at the liquid crystal layer. For sake of simplicity in the analysis, let the liquid crystal be placed at the incident light beam waist. Then we have

$$q_0 = iZ_{0f}(0) \equiv i \frac{\pi W_{0f}^2}{\lambda} \quad (9)$$

$Z_{0f}(0)$  indicates the confocal parameter of the incident gaussian light beam;  $W_{0f}$  is the corresponding radius of the beam waist; the light transmission matrix of the liquid crystal layer is as follows [2]:

$$\begin{bmatrix} \cos(\sqrt{x}d) & \sqrt{\frac{1}{x}} \sin(\sqrt{x}d) \\ -\sqrt{x} \sin(\sqrt{x}d) & \cos(\sqrt{x}d) \end{bmatrix}; \quad x \equiv 2c_2/c_1 \quad (10)$$

The light matrix from the liquid crystal output terminal to the

pinhole ( $z=1$ ) is

$$\begin{bmatrix} 1 & (l-d) \\ 0 & 1 \end{bmatrix} \approx \begin{bmatrix} 1 & l \\ 0 & 1 \end{bmatrix}$$

Thus, the transmission matrix of input/output is

$$\begin{aligned} \begin{bmatrix} A & B \\ C & D \end{bmatrix} &= \begin{bmatrix} 1 & l \\ 0 & 1 \end{bmatrix} \\ &\begin{bmatrix} \cos(\sqrt{x}d) & \sqrt{\frac{1}{x}} \sin(\sqrt{x}d) \\ -\sqrt{x} \sin(\sqrt{x}d) & \cos(\sqrt{x}d) \end{bmatrix} \\ &= \begin{bmatrix} \cos \sqrt{x}d - l\sqrt{x} \sin(\sqrt{x}d) & \\ -\sqrt{x} \sin(\sqrt{x}d) & \end{bmatrix} \\ &\begin{bmatrix} \sqrt{\frac{1}{x}} \sin(\sqrt{x}d) + l \cos(\sqrt{x}d) \\ \cos(\sqrt{x}d) \end{bmatrix} \end{aligned}$$

Since there is always  $c_2 < c_1$ ,  $\sqrt{x}d \ll 1$ , the above-mentioned equation is simplified to become:

$$\begin{aligned} \begin{bmatrix} A & B \\ C & D \end{bmatrix} &\approx \begin{bmatrix} 1-lxd & d+l \\ -xd & 1 \end{bmatrix} \\ &\approx \begin{bmatrix} 1-lxd & l \\ -xd & 1 \end{bmatrix} \end{aligned} \quad (11)$$

In addition,

$$\frac{1}{q_i} = \frac{1}{R_i} - \frac{i\lambda}{\pi W_i^2} \quad (12)$$

From Eqs. (8), (9), (11), and (12), we obtain

$$R_i = \frac{l^2 + Z_{cf}^2(0) \cdot (1-lxd)^2}{1 - Z_{cf}^2(0)xd(1-lxd)} \quad (13)$$

$$W_i^2 = \frac{\lambda}{\pi Z_{cf}(0)} \cdot [l^2 + (1-lxd)^2 Z_{cf}^2(0)] \quad (14)$$

Let the denominator of Eq. (13) be set equal to 0. We obtain:

$$l_0 = \frac{x d Z_{cf}^2(0)}{1 + x^2 d^2 Z_{cf}^2(0)} \quad (15)$$

By substituting Eq. (15) into Eq. (14), we obtain

$$W_0^2 = \frac{\left( \frac{\lambda Z_{cf}(0)}{\pi} \right)}{1 + x^2 d^2 Z_{cf}^2(0)} \quad (16)$$

In the following, the results are discussed.

1. The light (external) self-focussing without feedback

Let  $|B|=0$  (without feedback)

$$x = 2 c_2 / c_1 \cong \frac{b d^2 (\Delta \epsilon) \sin 2 \phi_0 |A|^2}{24 \pi K W_f^2(0) n_e(\phi_0)}$$

In the equation,  $|A|^2 = |E_{0f}|^2$  is proportional to the light intensity at the center of the incident light. For the liquid crystal materials PCB, MBBA or EBBA,  $(\Delta \epsilon) > 0$ ,  $b > 0$ ,  $x > 0$ ; from Eqs. (15) and (16), when  $x=0$  ( $|E_{0f}|^2=0$  or  $\phi_0=0$ ), the position and size of the beam waist do not change; conversely, when  $x$  gradually increases, the output beam waist contracts. Obviously, the phenomenon originates from the  $x$ -node self-focusing effect of the gaussian light beam by the refractive index squared distribution medium.

2. Optical bistability with feedback

Expand Eq. (14):

$$W_f^2 \cong \frac{\lambda}{\pi Z_{cf}(0)} [(l^2 + Z_{cf}^2(0)) - 2 l d Z_{cf}^2(0) x] = c_3 - c_4 x \quad (17)$$

In the equation,

$$\begin{cases} c_3 > 0 \\ c_4 > 0 \end{cases} \quad (18)$$

From Eqs. (10), (7), and (3), we obtain

$$\alpha \cong \frac{2c_2}{c_1} \cong \frac{bd^2(\Delta\epsilon) \sin 2\phi_0}{24\pi K n_e(\phi_0)} \times \left[ \frac{|A|^2}{W_f^2(0)} + \frac{|E_{0b}|^2 \cdot W_0^2}{W_b^2(0)} \right] \quad (19)$$

In the equation,  $|A|^2 = |E_{0f}|^2$  is determined by the intensity of the incident light. Similarly,  $|E_{0b}|^2 \cdot W_0^2$  is the single-valued function of the intensity of the incident light. The following is easy to prove:

$$\begin{cases} |A|^2 \cdot W_0^2 = 16 P_i / (1 - e^{-2}) \cdot cn \\ |E_{0b}|^2 \cdot W_0^2 = 16 P_i \cdot R / (1 - e^{-2}) cn \end{cases} \quad (20)$$

In the equation,  $P_i$  is the intensity of the incident light;  $W_{0f}$  and  $W_0$  are, respectively, the incident and the output beam waist;  $R$  is the reflective index of the reflector lens. Therefore, the variation of the size  $W_b(0)$  of the reflective light spot determines the optical bistability effect. For simplicity in analysis, it is assumed that the position of the reflector lens is fixed at the beam waist  $l_0$  (in the experiment,  $M$  is placed near the focus in front of a convergent lens). From the reverse-direction transmission matrix

$$\begin{bmatrix} 1 & l_0 \\ 0 & 1 \end{bmatrix}$$

and [ABCD] law,

$$q_b(0) = q_b(l_0) + l_0, \quad q_b(l_0) = i\pi W_0^2 \lambda, \quad \frac{1}{q_b(0)} = \frac{1}{R_b(0)} - \frac{i\lambda}{\pi W_b^2(0)}$$

By utilizing Eq. (16), we obtain

$$\frac{1}{W_l^2(0)} \cong \left[ \frac{\pi Z_{cf}(0)}{\lambda} \right]^2 \frac{1}{[l_0^2 + Z_{cf}^2(0)]^2} \times \left[ 1 + \frac{2d^2 Z_{cf}^2(0) (Z_{cf}^2(0) - l_0^2)}{(Z_{cf}^2(0) + l_0^2)} x^2 \right] \quad (21)$$

By substituting Eqs. (19) through (21), we have

$$W_l^2 = c' - c'' x^2 \quad (22)$$

In the equation,

$$\begin{aligned} c' &= c_3 - \frac{c_4 b d^2 (\Delta \epsilon) \sin 2\phi_0}{24 \pi K n_e(\phi_0)} \\ &\times \left[ \frac{16 P_i}{(1 - e^{-2}) c n W_l^2(0)} + \frac{16 P_i R}{(1 - e^{-2}) c n} \right. \\ &\left. \times \left( \frac{\pi}{\lambda} \right)^2 \left( \frac{Z_{cf}(0)}{l_0^2 + Z_{cf}^2(0)} \right)^2 \right] \\ c'' &= \frac{c_4 b d^2 (\Delta \epsilon) \sin 2\phi_0}{24 \pi K n_e(\phi_0)} \cdot \frac{16 P_i R}{(1 - e^{-2}) c n} \\ &\times \left( \frac{\pi}{\lambda} \right)^2 \left( \frac{Z_{cf}^2(0)}{l_0^2 + Z_{cf}^2(0)} \right)^2 \\ &\times \frac{2d^2 (Z_{cf}^2(0) - l_0^2)}{(Z_{cf}^2(0) + l_0^2)} \end{aligned}$$

Eqs. (17) and (22) are conditions determining the optical bistability. Let

$$c_3 - c_4 x = c' - c'' x^2,$$

When  $c''=0$  (without light feedback), since  $c_3 > c'$ ,  $c_4 > 0$ , there is a stability solution  $x$  in the light self-focusing situation. If there is feedback but the input light energy  $P_i$  is relatively small, that is  $c''$  approximates 0, it is impossible to insist that the second solution corresponds to  $W_l^2 < 0$ . Therefore, in this case the bistability phenomenon does not exist, as shown in Fig. 3

(a). Conversely, when the input light intensity is high enough so that  $c''$  is very large, but  $c'$  is very small, it is possible to have the discriminant equation  $\Delta = c_3^2 - 4c''(c_3 - c') < 0$ . Now there is no stability solution with the appearance of oscillating output light. This corresponds to intensive positive feedback, as shown in Fig. 3 (c). The condition for the appearance of optical bistability is  $\Delta > 0$  and  $\sqrt{c'/c''} < c_3/c_4$ , that is,  $\frac{c_3^2}{4(c_3 - c')} > c'' > c' \left( \frac{c_4}{c_3} \right)^2$ .

The above-mentioned equation determines the range of input light for producing optical bistability, as shown in Fig. 3 (b).

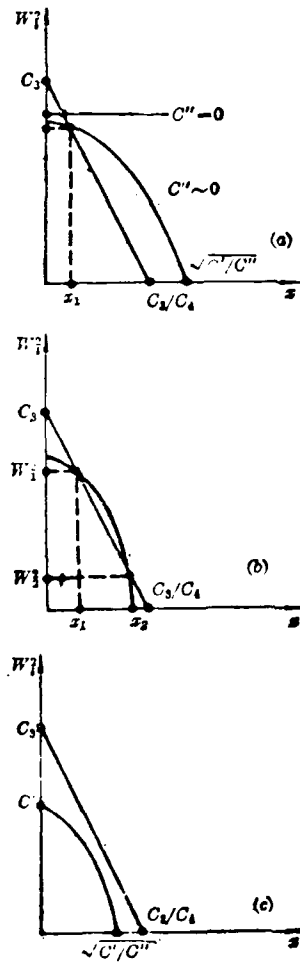


Fig. 3

Remark: (a) single stability (b) bistability  
(c) without stability

## II. Experimental Observations

Fig. 4 shows the experimental arrangement. The specimen was EBBA. The laser used was a continuous-wave  $\text{Ar}^+$  laser with wavelength 514.5nm, single-mode output, power above 5W, that was continuously adjustable. The lens  $f_1$  allowed the input light beam waist falling near the specimen. The feedback plane semi-length ( $R$  is approximately 95%)  $M$  is placed near the front focus of the second lens  $f_2$ . The output light beam 1 and the reference light beam 2 (coming from the  $\text{Ar}^+$  laser) simultaneously entered the x-y recorder. In the experiment, the variation of  $P_i$  was relatively slow. Measurements were taken at different temperatures; the isothermal control was  $\pm 0.5^\circ\text{C}$ . Restricted by the isothermal furnace, the  $\phi_0$  angle was  $8^\circ$ .

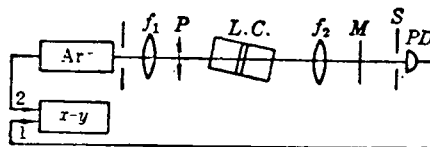


Fig. 4. Experimental arrangement

When  $f_2$  and  $M$  are eliminated, the input/output curve is shown as in Fig. 5 without the appearance of bistability. After the input power  $P_i$  exceeds 200mW, the input/output appears in an apparent nonlinear relationship. After the power is continuously raised to 1W, the output light intensity increases and decreases. In the experiment, the authors observed size contraction and expansion effects in the light spots.

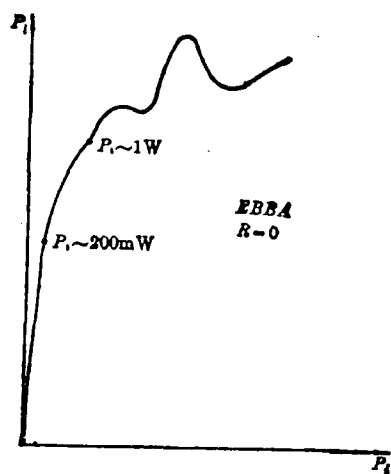


Fig. 5

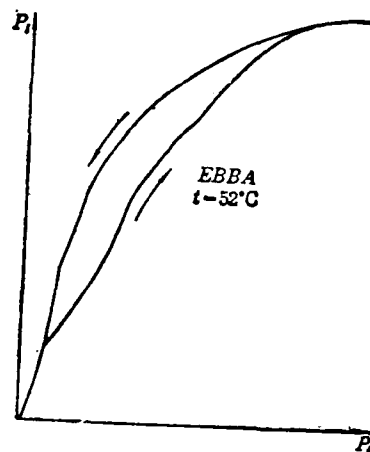


Fig. 6

Fig. 6 shows the input/output curves ( $t=52^{\circ}\text{C}$ ) after adding light feedback. When  $P_i$  exceeds a certain value, the apparent phenomenon of optical bistability appears.

At room temperature (crystalline phase) or when the specimen is rotated so that its polarization is in a position perpendicular to the surface of the paper (normal light ray) the above-mentioned experimental phenomenon disappears. This proves that the origin of the light self-focusing and optical bistability is the photo-reorientation effect toward phase array.

The above-mentioned experimental phenomena and the theoretical analysis are qualitatively consistent.

This research subject was funded by the Fujian Provincial Science Foundation. In addition, the authors are grateful to the Anticancer Center of Xiamen University for providing experimental equipment, and to comrade Li Yingling for sealing the experimental specimens.

This paper was received on 26 January 1988.

REFERENCES

1. Khoo, I.C., Phys. Rev. A 25, 1630 (1982).
2. Yariv, A., Quantum Electronics, 175, pp. 112-113.
3. Born, M. and E. Wolf, Principles of Optics, 1975, p. 680.

## BINOCULAR STEREOSCOPIC HOLOGRAMS FOR THREE-DIMENSIONAL DISPLAY

Kang Hui and Yang Yingmin, Department of Physics, Nankai University, Tianjin

**Abstract:** The paper discusses and presents high-efficiency stereoscopic holograms in the near-image plane. Under natural light indoors, bright stereo images can be observed; in addition, the paper analyzes some problems related to stereo images.

**Key technical terms:** three-dimensional display, binocular stereoscopic holograms.

### I. Introduction

Three-dimensional imaging technology is a research topic that is receiving attention aimed at finding a solution. To implement the recording and display of three-dimensional spatial data, researchers have developed two types of three-dimensional imaging techniques [1]: one is the binocular stereo-imaging technology, and the other is the holographic imaging technology. In recent years, scientists combined these two imaging techniques to develop a new three-dimensional display technique [3]. In this technique a set of transparencies containing parallax is used as the object; an optical method is used to record the information into stripe-transmission Fresnel holograms, which are called composite holograms. To observe the holograms, no attachments are needed to produce an animated three-dimensional

image, since the human eyes execute relative motion with regard to the hologram. Obviously, this technique has the advantage of being capable of recording a hologram of any scene; however, there are some drawbacks. For example, with this technique special recording equipment is needed in recording large numbers of holograms with stereo-films; a point light source is required for observation during the reconstruction of the image because the single-element hologram is a narrow stripe in shape, thus limiting the resolving power of the reconstructed image.

The paper utilizes holograms that have the property of multiple recording and reconstructions; on a single film of the recording medium, two transparencies are recorded at the same time as the near-image plane holograms with certain parallax information. These are binocular stereoscopic holograms. During reconstruction, an observer is required to be at an appropriate position to be able to observe an image with his eyes without any attached equipment, thus achieving stereo vision. Compared with the composite hologram, an obvious distinction between the two methods is that only two hologram transparencies are recorded; these holograms are not the separate narrow stripe-shaped Fresnel holograms, but near-image-plane holograms that mutually overlap. Therefore, in addition to the advantage of composite holography this technique overcomes the shortcoming of composite holography, but with the property of high utilization rate of light energy. On many occasions, especially in nondestructive testing, this property has a major potential of application.

The paper describes in detail a method of comprehending binocular holograms, deduces and derives formulas of the amplification ratio of binocular stereo-holograms, and it analyzes and discusses some problems in reconstruction observation. A DCG board was used to record the highly efficient binocular stereoscopic holograms of the reflective image plane.

In this method, no special illumination is required; the bright stereo images can be observed in natural indoor illumination.

## II. Comprehending Binocular Stereoscopic Holograms

The making of binocular stereoscopic holograms proceeds in two steps: 1. photographing a pair of stereograms; and 2. comprehending the binocular stereoscopic hologram.

1. Photographing a stereo-film pair: the stereo film pair is a positive transparent film pair of an object photographed from different directions with a camera; the films include the parallax information. From Fig. 1, the displacement variation reflecting the magnitude of parallax can be derived:

$$\begin{aligned}\Delta x = x_1 - x_2 &= M_1 B \frac{\Delta L}{L} \cos \theta \\ &= f' B \frac{\Delta L}{L^2} \cos^2 \theta\end{aligned}\tag{1}$$

In the equation,  $f'$  is the focal length of the camera,  $B$  is the length of the baseline that is photographed,  $L$  is the vertical distance from the point of collimation to the baseline;  $\Delta L$  is the special depth from the collimated point to another point;  $M_1$  is the amplification ratio of the vertical axis of the collimated plane, and  $2\theta$  is the included angle of the two axes of the photographed object. From the above-mentioned equations, on the photographed stereo films, the displacement of the above-mentioned point is proportional to the square of the following parameters: focal length of the camera, length of the baseline that is photographed, and cosine of the included angle of the line of sight, and inversely proportional to the square of the distance from the collimated point.

2. Comprehending the binocular stereoscopic hologram: The stereoscopic binocular hologram involves a grasp of binocular stereoscopy and holography. Based on their principles, a

binocular stereoscopic hologram should have the following properties: a. The reemergent pupil should be the real-image point of suppression; the spacing between the two is approximately equal to the interpupillary distance; b. both of the reemergent image brightness are approximately equal; c. the spacing of the observation should be greater than the distance of distinct vision. Fig. 2 shows the reemergent principle of the binocular stereoscopic hologram.

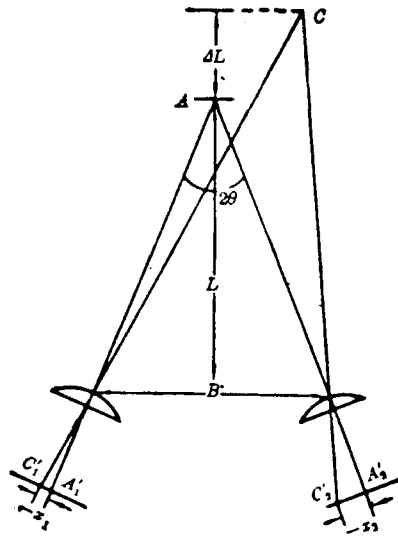


Fig. 1. Photographing of stereo transparency pair

Fig. 3 shows the arrangement for recording a binocular stereoscopic hologram. In Fig. 3, A is the laser, SP is the beam splitter, L is the convergent lens, P is the pinhole, M is the reflecting lens, D is the diffuse scattering screen,  $L_1$ ,  $L_2$  are the imaging lenses,  $O_1$ ,  $O_2$  are the stereoscopic transparency pair, and H is the holographic recording material. The lens  $L_1$  forms an image at  $L_2$  from the point light source, thus providing a convergent illuminating light; the diffuse scattering body

diffuses the convergent point source to fill the aperture  $d$  of the lens  $L_2$ , which forms an image in the recording plane  $H$  with the transparencies  $O_1$  and  $O_2$ . From different directions, reference light beams are introduced to record the near-image-plane stereoscopic hologram. In Fig. 3, the dotted line is the reference light path for recording the transmission hologram; the reference light path is perpendicular to the light connecting the two lenses  $L_2$ , but the path does not lie within the plane of the paper, but within the symmetric bisecting plane of the included angle of the two object light beams, thus ensuring that the direction in which color dispersion of the diffracted light occurs is perpendicular to the baseline of the viewer's eyes. The solid line shows the reference light beam of the stereoscopic hologram for recording the reflective image plane. Except for the incidence from the back plane, the other situations are similar to transmissions. However, owing to very high selectivity of wavelength because of diffraction, the reflective body is holographically reemergent approximately as a monogram of the image light beams. Therefore, the direction of the reference light may not be limited as mentioned above; the reference light may fall within the same plane as that of the two object light beams. To satisfy the general requirements of the stereoscopic holograms of both eyes, the length of the line connecting the centers of the two  $L_2$  lenses should be equal to the interpupillary distance  $b$  (approximately 65mm). The vertical distance  $l$  from the connecting line to  $H$  should be greater than the distance of distinct vision.

### III. Reemergence and Observation of Binocular Stereoscopic Hologram

Photographed with Fig. 3 is the near-image-plane binocular stereoscopic hologram; during reemergence, a conjugate reference light path should be adopted, as shown in Fig. 4. In Fig. 4 (a) and (b) there are indicated, respectively, the reemergence of two

situations of transmission and reflection. In the following, several problems are discussed concerning reemergence.

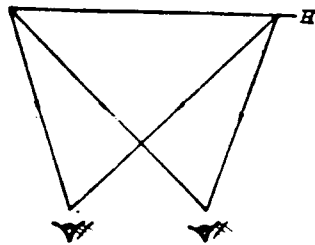


Fig. 2. Reemergence of binocular stereoscopic hologram

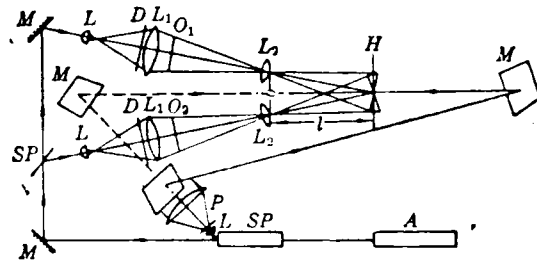


Fig. 3. Optical system for comprehending a binocular stereoscopic hologram

### 3.1. Stereoscopic amplification ratio

Through a stereoscopic hologram, the observed reemergent three-dimensional scene is different stereoscopically from direct observation of the scene. A description of this variation can be compared in the two following aspects.

A. By comparing the discrimination capability of the depth difference of the positions of various object points in the three-dimensional scene, the ratio  $\Delta x$  (physiological parallax) generated by the corresponding two points can be used as an indication; this is called the stereoscopic amplification ratio. From Eq. (1) it can be derived that the three-dimensional parallax generated by the reemergent image of the binocular stereoscopic hologram observed by the human eye is as follows:

$$\Delta x' = M_2 B f' f'_e \Delta L \cos^2 \theta' / (L^2)$$

In the equation,  $M_2$  is the amplification ratio of  $L_2$  with respect to the transparency when recording the hologram,  $f'_e$  is the focal length of human eyes, and  $l$  is the observation distance. At the camera position in making the photograph, with three-dimensional parallax the human eye directly observes the scene.  $\Delta x_0 = b f'_e \Delta L \cos^2 \theta' / L^2$

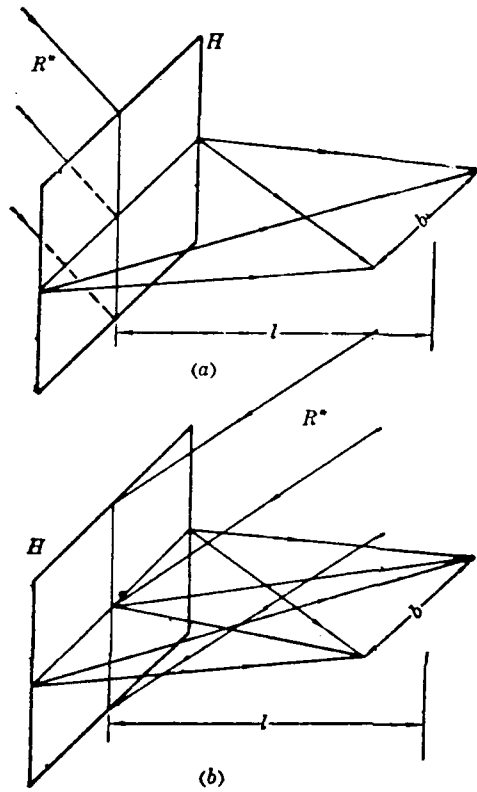


Fig. 4. Reemergence light path of binocular stereoscopic hologram  
 Remark: (a) Transmission reemergence  
 (b) Reflection reemergence

In the equation,  $2\theta'$  is the included angle of the line of sight of both eyes and  $b$  is the length of the baseline of both eyes. Then the stereoscopic amplification ratio  $P$  is as follows:

$$P = \frac{\Delta x'}{\Delta x_0} = M_2 \cdot \frac{B}{b} \cdot \frac{f'}{l} \cdot \frac{\cos^2 \theta}{\cos^2 \theta'}$$

From the equation, by selecting the photograph parameters  $B$ ,  $\theta$ , and  $f'$  and recording the parameter  $l$ , we can let  $P > 1$ ; thus, the

resolving power can be increased to the depth difference of a three-dimensional scene.

B. Concerning the variation ratio of the special depth, the inverse proportion of the depth difference of two corresponding points between the actual three-dimensional scene and the three-dimensional scene with reemergence by using the hologram can be used as an indication:

$$\Delta l / \Delta L = M \cdot B / b \cdot l / L \cdot \cos \theta' / \cos \theta$$

In the equation,  $M=M_1M_2$ , indicating the lateral-direction amplification ratio between the reemergent scene and the actual scene. From the equation, since generally the ratio is smaller than 1, the three-dimensional image reemerged with the hologram has less depth sense than that of the actual scene.

### 3.2. Observation range of the reemergent image

When a person observes a reemergent image through a binocular stereoscopic hologram, both his eyes should be positioned within a limited range in order to grasp the three-dimensional scene. Fig. 5 (a) shows a top view of the holographic reemergent optical path; two penumbral zones in the figure represent the range within which a single complete image can be observed. Therefore, when both eyes are positioned, respectively, in these zones, one or both eyes can observe a single image in generating a three-dimensional image. Otherwise, only a plane image can be observed. Fig. 5 (b) is a side image exhibiting the emergence of the hologram; the solid lines in the figure indicate the reemergence of the reflective hologram with only diffractive monochromatic pupil. However, the entire figure (b) (including solid lines and dotted lines) indicates the reemergent polychromatic pupil of the transmission hologram.

### 3.3. The effect of light source on reemergent observation

Since the recorded binocular stereoscopic hologram is of the near-image-plane type, the requirement on the reemergent illuminating light source will be considerably reduced; this property of the binocular stereoscopic hologram is better than that of a composite hologram. When the illuminating light source deviates from the original reference light source along the axis,

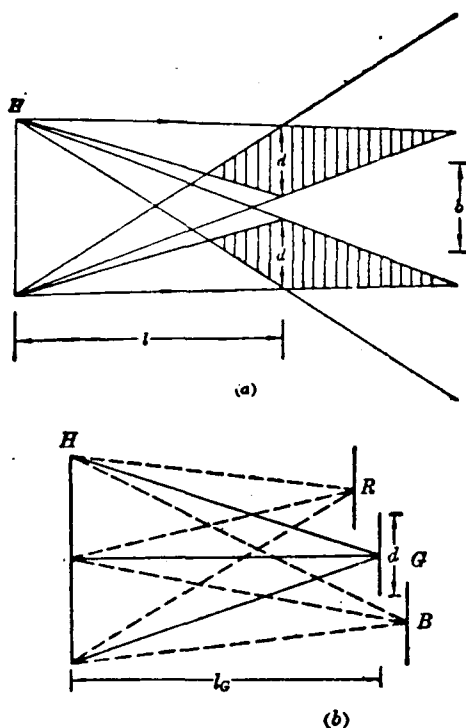


Fig. 5. Spatial range in which both eyes should be located in order to generate three-dimensional vision when directly observing the reemergent vision of a hologram

in addition to variation of the position and size of the reemergent pupil, the others are not significantly changed. Fig. 6 shows the variation in position and size of the reemergent pupil when the illuminating light source changes from parallel light to a point source at  $2l$  from the hologram. When the

illuminating light source deviates from the original reference source along the vertical axis, the selectivity of angles of the hologram will reduce the brightness of the diffraction image.

This factor can be used in illuminating the hologram with a plane light source, so as not to have the phenomenon of the overlapping of two reemergent pupils. This also reduces the requirement of the illuminating light source; the authors' experimentation proved this point. The holograms constructed by the authors can be used to observe better three-dimensional images, whether illuminated with a point source or a plane source (such as a 40W daylight light, using indoor natural light).

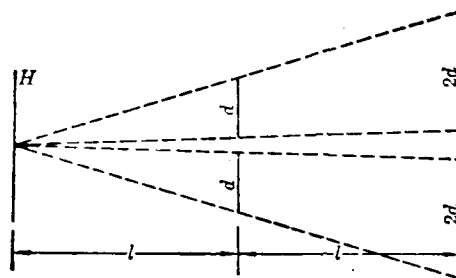


Fig. 6. Effect on reemergent pupil when the axial position of the reemerging point source is varied

#### IV. Experiments and Results

The experimental arrangement used by the authors for recording the binocular stereoscopic holograms is a variant of Fig. 3. In the experimental arrangement,  $L_1$  is the collimating lens that generates parallel light to illuminate the object transparency  $O$ . Lens  $L_2$  generates an image of  $O_1$  at  $H$ ; in addition, at the back focal plane of  $L_2$ , a Fourier spectrum of  $O$  is formed; the vertical distance (of the spectral plane from  $H$ )  $l=300\text{mm}$ . In the experimental arrangement, no diffuse scattering screen is included; however, since the point source is of a certain size and the transparency has some diffuse scattering

capability, the spectrum of the transparency is slightly expanded. Furthermore, since the transmission hologram is easier to make than the reflection hologram, the authors comprehended the reflection-type binocular stereoscopic holograms. The reference light used is shown by the solid lines in Fig. 3. To achieve high diffraction efficiency, the authors used DCG as the recording medium. There are two types of light exposure: A. sequential (one repetition) light exposure method, and B. simultaneous (single-time) light exposure method. The reference object ratios of the two situation differ; in addition, the one-repetition light exposure of the sequential method is also slightly different. With the experiment, satisfactory results were obtained with both hologram recording methods. The effective dimensions of the holograms are 80mm square, with a very high diffraction efficiency. The conventional white light source was used in illumination. For example, a very bright three-dimensional image can be observed with an 8W daylight lamp. With indoor illumination of natural diffuse scattering light incident from a window during overcast weather, a bright three-dimensional image can be observed. The depth sense of the image will vary with the observation distance  $l$ .

As introduced in the paper, this is a simple and easily carried out method of comprehending a binocular stereoscopic hologram. Owing to the high resolving power of the reemergent three-dimensional image and the discrimination rate of spatial depth, the binocular stereoscopic holograms are used in X-ray three-dimensional film in industry and medicine to comprehend three-dimensional transparency images in order to discover anomalies inside an image (as the so-called nondestructive testing); this is very significant. In addition, binocular stereoscopic holograms have extensive applications in advertisements, education and artificial expression; therefore, the technique is worthy of promotion.

This paper was received on 9 November 1987.

REFERENCES

1. Okoshi, T., Three-Dimensional Image Techniques, Academic Press, New York, (1976).
2. Yu Tao, Yingyong Guangxue [Applied Optics], Science Publishing House, (1966).
3. Yu Meiwen, Guangxue Quanxi Ji Xinxi Chuli [Optical Holography and Information Processing], Defense Industry Publishing House, (1983).

## STUDY OF PHOSPHATE LASER GLASS WITH HIGH NEODYMIUM CONCENTRATION

Mao Hanfen, Mao Sen, Li Jie, Jiang Yanyan, and Jiang Yasi,  
Shanghai Institute of Optics and Fine Mechanics, Chinese Academy  
of Sciences, Shanghai

**Abstract:** In the paper, two systems of high-neodymium-concentration phosphate laser glass of  $\text{Li}_2\text{O-Nd}_2\text{O}_3\text{-La}_2\text{O}_3$  and  $\text{R}_2\text{O-RO-Nd}_2\text{O}_3$  are developed; in addition, their physicochemical and spectral properties and laser features were determined. Laser rods of OD4x60mm were fabricated; when the input was 32J, the output was 448mJ.

**Key technical terms:** high-neodymium-concentration, phosphate.

### I. Introduction

In ordinary laser materials doped with neodymium, interaction with neodymium ions will cause quenching of relatively high-concentration fluorescence. Therefore, the dopant concentration of neodymium ions in the substrate is generally considered as not exceeding  $2 \times 10^{20} \text{cm}^{-3}$ . However, in recent years it was discovered that the  $\text{Nd}^{3+}$  concentration in neodymium-doped crystals may be as high as  $4 \times 10^{21} \text{cm}^{-3}$ , but fluorescence quantum efficiency is not appreciably reduced. Furthermore, researchers proved that it is feasible to quench low-concentration fluorescence in high-neodymium-concentration phosphate glass [1]. Therefore, high-neodymium-concentration

doped materials were gradually emphasized by researchers. Of interest to researchers is that a new pathway was opened for developing high-efficiency repetition pulse laser systems by relying on increasing the concentration of excited ions and raising the excited-emission cross section  $\sigma$ , in order to reduce the dimensions of the excited components; the fairly high heat migration rate is due to the small dimensions. The paper reports on two systems of high-neodymium-concentration phosphate glass with the results from measurement and tests to determine the constituents, preparation techniques, as well as some physicochemical and laser properties. HNG-23 glass was patented, since it has high laser efficiency for use as the working medium of small-size lasers.

## II. Constituents and Properties

Two systems were selected: one is glassy-state tetrphosphate  $(\text{Li-Nd}_x \cdot \text{La}_{1-x})\text{P}_4\text{O}_{12}$ . The other is crystal-state lithium neodymium tetrphosphate  $\text{LiNdP}_4\text{O}_{12}$ , a high-efficiency laser crystal. However, the preparatory techniques for this kind of crystals are difficult, given its small dimensions and low optical quality. However, through preparatory techniques the glassy-tetrphosphate can be made to surmount these disadvantages. Another type of system is the heat-resistant glass  $\text{R}_2\text{O-RO-Nd}_2\text{O}_3\text{-P}_2\text{O}_5$  high-neodymium-concentration superphosphate system.

Applied in pulse repetition lasers, in a phosphate laser the glass should have a low heat effect (small variation, or a nearly-zero variation, in optical paths owing to thermal expansion with variation in temperature along with the refractive index and birefringence) in addition to more satisfactory laser parameters as well as physicochemical and optical properties.

After the above-mentioned overall considerations, heat-resistant glass was prepared with the following range of constituents (mole percent):  $P_2O_5$  60 to 70%,  $R_2O$  5 to 12%,  $RO$  10 to 25%, and  $(Al_2O_3 + Nd_2O_3)$  2 to 10%; in addition, a small amount of anti-aging additive was added. In these constituents,  $R_2O$  and  $RO$  are oxides of alkali metals and alkaline-earth metals.

Glass of the two above-mentioned systems uses highly purified and high-grade starting materials, with blending according to the proportions of the chemical constituents. After blending, the material being compounded first undergoes a preliminary reaction with melting, in a two-step method: first the compounding material is melted in a quartz crucible into the treated material before homogenization and clarification in a platinum crucible. The molten glass is annealed and is precisely processed into specimens, which are measured and tested for various properties.

For the first category  $LiNd_xLa_{(1-x)}P_4O_{12}$  system glass, its physicochemical and spectral properties were measured, in general; see Table 1 for results. The spectral and luminance properties of this type of glass were described in published papers [2]; therefore, these properties are not mentioned here. From Table 1, this type of glass is seen to have a pronounced crystallization tendency. In the preparatory process, the authors adopted the precombustion method for the compounded materials in order to reduce volatility of  $P_2O_5$ , thus improving the crystallizability of the glass. It should be pointed out, in addition, that after the specific dehydration technique was used by the authors [3], the moisture content in the glass apparently decreased. Measurements showed that the absorption coefficient  $K_{OH} < 1\text{cm}^{-1}$  for all type OH radicals near 3.3 micrometers in the near-infrared zone; this absorption coefficient is lowered by one-quarter of its value compared to conventional phosphate glass, thus ensuring practicality of this type of glass.

TABLE 1. Some Properties of  $\text{LiNd}_x\text{La}_{(1-x)}\text{P}_4\text{O}_{12}$  System Glass

玻璃牌号 <sup>1</sup>	$2. \text{Nd}^{3+}$ 浓度 ( $\times 10^{21} \text{cm}^{-3}$ )	$n_D$	密度 $d$ 3 ( $\text{g}/\text{cm}^3$ )	热膨胀系数 <sup>4</sup> $\alpha \times 10^{-7} \text{C}^{-1}$	析晶性质 (保温 1 小时) <sup>5</sup>	寿命 <sup>6</sup> $\tau$ (us)
HNG-1	0.83	1.5840	3.16	100	1250~1300°C 7全透 1200~1160°C 9表面失透 1160~810°C 8全失透	100
HNG-2	1.33	1.5835	3.10	98	1250~1170°C 7全透 1170~1100°C 9表面失透 1100~810°C 8全失透	95
HNG-3	2.01	1.5811	3.07	97	1250~1165°C 7全透 1165~1080°C 9表面失透 1080~810°C 8全失透	80
HNG-4	2.65	1.5800	3.09	95	1250~1120°C 7全透 1120~810°C 8全失透	60
HNG-10	2.98	1.5772	3.10	98	1250~1110°C 7全透 1110~810°C 8全失透	50
HNG-8	4.0	1.5803	3.17	93	1250~1140°C 7全透 1140~810°C 8全失透	30

KEY: 1 - Grade of glass 2 - Concentration of  $\text{Nd}^{3+}$  ( $10^{21} \text{cm}^{-3}$ ) 3 - Density  $d$  ( $\text{g}/\text{cm}^3$ ) 4 - Coefficient of thermal expansion  $\alpha \times 10^{-7} \text{C}^{-1}$  5 - Property of crystallization (1h at constant temperature) 6 - Service life  $\tau$  ( $\mu\text{s}$ ) 7 - Completely transparent 8 - Completely opaque 9 - Opaque service

Table 2 lists some physicochemical and optical properties of the  $\text{R}_2\text{O}-\text{RO}-\text{Nd}_2\text{O}_3-\text{P}_2\text{O}_5$  system-based heat-resistant glass.

The following shows the results of the determination (acid-resistant and moisture-resistant tests) of the chemical stability of the glass:

Acid-resistant properties: according to GB 903-65 State Standard Method, freshly buffed specimens were placed in 0.1N acetic acid at 50°C for 5h of reaction (the time required for the destruction depth of 135 micrometers at the buffed surface of the glass). pH 2.9 test fluid was used to examine HNG-2, HNG-22 and

HNG-23 specimens without displaying a purple-blue color; these specimens are of grade 1.

TABLE 2. Properties of  $R_2O-RO-(Al_2O_3 + Nd_2O_3)-P_2O_5$  Heat-Resistant Glass

玻璃牌号	1 2 $Nd^{3+}$ 浓度 ( $\times 10^{21} cm^{-3}$ )	$n_D$	3 密度 $d$ ( $g/cm^3$ )	4 热膨胀系数 $\alpha \times 10^{-7} ^\circ C^{-1}$	5 析晶性能(保温 1 小时)	6 寿命 $\tau$ ( $\mu s$ )
HNG-18	0.71	1.5512	2.93		1250~960°C 7 全透 960~810°C 9 表面失透	180
HNG-19	0.73	1.5425	2.75		1250~1090°C 7 全透 1090~810°C 8 全失透	160
HNG-20	0.74	1.5269	2.61		1250~1070°C 7 全透 1070~810°C 9 表面失透	140
HNG-22	0.75	1.5454	3.00	133(20°C·T)°C	1250~810°C 7 全透	180
HNG-23	1.91	1.5657	3.14	90(20°C~100°C)	1250~810°C 7 全透	160

KEY: 1 - Grade of glass 2 - Concentration of  $Nd^{3+}$  ( $10^{21} cm^{-3}$ ) 3 - Density  $d$  ( $g/cm^3$ ) 4 - Coefficient of thermal expansion  $\alpha \times 10^{-7} ^\circ C^{-1}$  5 - Property of crystallization (1h at constant temperature) 6 - Service life  $\tau$  ( $\mu s$ ) 7 - Completely transparent 8 - Completely opaque 9 - Opaque service

Moisture resistance: based on GB 903-65 State Standard Method, freshly buffed specimens were placed for 5h in a humidified atmosphere at 50°C and 85% relative humidity. When observed under an 80-power holographic microscope, no spots were discovered in all the three specimens mentioned above.

A determination of the laser parameters was made with a small-size laser, which is of the planar cavity type with repetition rate between 1 to 50pps. The light-focusing device is of the single-lamp elliptical cylindrical type; the lamp and rod were placed separately onto two focal lines of the elliptical cylinder; the length of the laser cavity was 330mm; the effective region of light pumping is OD4x50mm. Fig. 1 shows the results of

determining the laser efficiency and the threshold value of HNG-23 glass. From the figure, the threshold value of HNG-23 glass was 1.5J. When operating at ten times per second with 32J, the output energy was 448mJ. The laser efficiency was 1.40%.

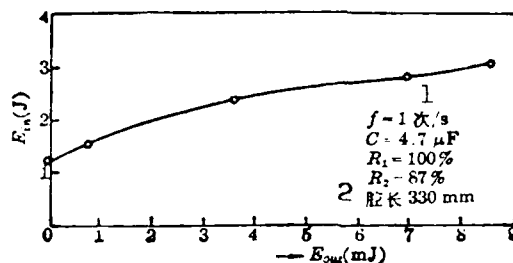


Fig. 1

KEY: 1 -  $f=1$  time per second 2 - cavity length 330mm

The paper was received on 30 March 1988.

#### REFERENCES

1. Danilmeye, H.G. and H.P. Weler, IEEE J. Quant. Electr. **QE-8**, 805 (1982).
2. Qi Changhong, and Gan Fuxi, Jiguang [Lasers] **9/11**, 691 (1982).
3. Zhuo Dunshui, Xu Wenjuan, and Jiang Yasi, Zhongguo Jiguang [Lasers in China] **12/3**, 173 (1985).

## STRESS-STRAIN STATE OF SLAB AMPLIFIERS

Ding Liming, Shanghai Institute of Optics and Fine Mechanics, Chinese Academy of Sciences, Shanghai; Yang Fumin, Shanghai Observatory, Chinese Academy of Sciences, Shanghai; S.R. Bowman, J. Fogleman, and C.O. Alley, University of Maryland, United States

**Abstract:** The stress-strain state of slab amplifiers was measured; sealing materials and the installation method were improved; a sealing material that does not induce stresses was developed.

**Key technical terms:** slab amplifier, stress and strain.

### I. Introduction

The development of a slab-shaped solid-state laser with a high pulse repetition rate and high power is a subject that is presently of interest to Chinese as well as foreign scientists [1]. To enable the slab amplifiers to withstand high power and high energy and, at the same time, to reduce birefringence and to improve laser output brightness, studying the stress-strain state induced in laser amplifiers is important. Furthermore, to improve the anti-explosion capability of slab amplifiers [2], in addition to factors of laser materials, an installation method that does not induce stress should be developed [3]. Therefore,

the authors designed four installation arrangements and improved the sealing materials and the installation method; better effects were realized.

## II. Experimental Arrangement and Experimental Results

Fig. 1 shows the measurement setup for the stress-strain state. Passing through a beam expanding device with a pinhole at the focus of the He-Ne laser, a beam was generated with its aperture at 35mm as a polarized, homogeneous light beam, which passes through a pair of polarized lenses with axes intersecting each other, a dark field was formed after exiting the polarized lenses. When the laser material was placed between two polarized lenses, anisotropy will be induced if an inhomogeneous force acts on the material. In this case, the light ray will have different speeds of propagation in two directions perpendicular to each other, thus producing a difference of optical paths. Therefore, bright bands appeared after exiting the polarized lenses. This phenomenon can be expressed as follows [4]:

$$\sigma_y - \sigma_x = \frac{n\lambda}{B \cdot d} \quad (1)$$

$\sigma_x$  and  $\sigma_y$  are the stresses along two directions;  $n$  is the band series;  $\lambda$  is the measured laser wavelength;  $B$  is a constant determined by the laser material;  $d$  is the thickness of the material in the  $z$ -direction.

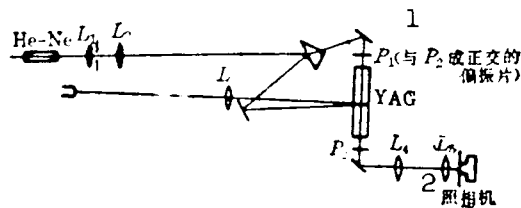


Fig. 1. Optical path diagram for measurement of the stress-strain state  
KEY: 1 -  $P_1$  indicates a polarized lens perpendicular to  $P_2$  2 - Camera

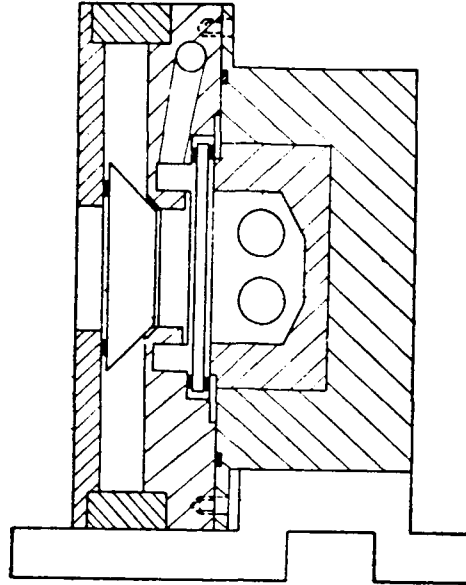


Fig. 2. Nd:YAG excited refractive type slab amplifier

To measure the stress-strain state, the authors conducted a stress state determination with an arrangement as shown in Fig. 2 by using model III silicate glass slab-shaped laser material prepared at the Shanghai Institute of Optics and Fine Mechanics. Fig. 3 shows a stress diagram of the original laser material; stresses at two corners were induced when the lateral surface of the neodymium glass was buffed. To reduce stresses, a special black material with ample elasticity was used to seal the lateral surface of the neodymium glass; Fig. 4 shows the manner of sealing. When the cover plate was pressed tightly (the plate hinders the laser) and when the bolts were pressed tightly on two components of the flashing light and laser material, the generated stress is shown separately in Figs. 5(a) and (b).

To plan how to eliminate the stresses, the second setup

designed by the authors was not tightened and sealed with bolts, but with intact pieces of plastic slabs. Two slabs were placed at each terminal of the slab amplifier; between two slabs, silica gel with good elasticity was placed as sealant. Fig. 6 shows the sealing mode. However, since two corners of the glass slab were sealed, contraction resulted after the silica gel dried. Therefore, extra stresses were generated at the corners.

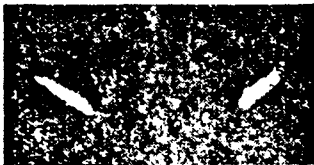


Fig. 3

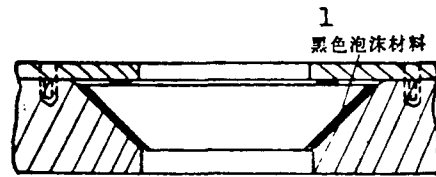


Fig. 4. Schematic diagram of manner of sealing  
KEY: 1 - Black forming material

In the third setup designed by the authors, two corners of the slab-shaped glass were loosened; silica gel was used to seal the bottom of two sides of the slab, and the edge of the bottom, as shown in Fig. 7. Because the silica gel contracted, however, stresses were induced at both sides and the base of the glass material.

In the fourth setup designed by the authors, a kind of glue that does not contract was used; only the base of two sides of the glass slab adhered to the glue, as shown in Fig. 8 (a) and (b). Made by the Corning Corporation in the United States, No. 186 elastic glue meets this requirement. As shown by measurements, no extra stresses were induced in the glass slab after installation; stresses were induced only after the cooling water is connected. After a face panel was added in front of the glass slab, no stresses were induced (Fig. 9(a)); the stresses induced after the water was connected were smaller than the

stresses in the case when the face panel was not added (see Fig. 9 (b)); this is because the pressure on the face panel had a certain balancing function on the hydraulic pressure. When the light pumping input was 2645W, 5Hz, the corresponding stresses are shown in Fig. 9 (c). In the experiments, no damage to the glass was observed.



Fig. 5

Remark: (a) The installation stress diagram (addition of face panel) of the first setup  
 (b) The installation stress diagram (after turning the bolts tightly) of the first setup

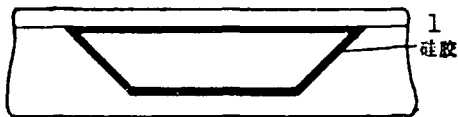


Fig. 6. Schematic diagram showing sealing mode  
 KEY: 1 - Silica gel

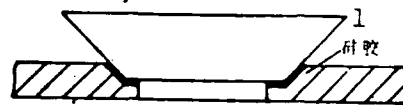


Fig. 7. Schematic diagram showing sealing mode  
 KEY: 1 - Silica gel

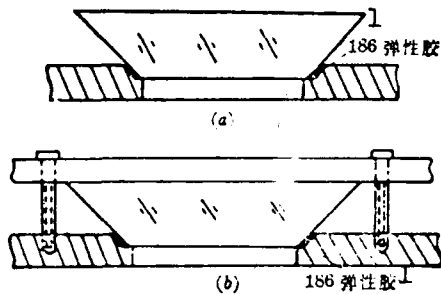


Fig. 8. Schematic diagram of sealing mode  
 KEY: 1 - No. 186 elastic glue

Finally, the YAG slab with the same dimensions was installed; its stresses were measured. Since YAG material is much harder than glass, the stress variation was much smaller than that of glass; no stresses were induced after installation. No added stresses were induced even after cooling water was connected; see Fig. 10 (a) and (b).

### III. Analysis of Experimental Results

From the experimental measurements it can be seen that the stresses induced by the material are related, to a great extent, to the material properties, shape, processing requirements, mechanical design of the material placement, manner of installation, and properties of sealing material. Mainly, the authors improved the installation method and used sealing materials that do not contract. Therefore, no stresses were induced after installation.

Theoretically, the limiting power of a unit volume of input that the slab material can withstand is as follows [5]:

$$P_{\max} = \frac{12 R_g}{x t^2} \quad (2)$$

In the equation,  $R_g$  is the heat impact parameter;  $x$  is the ratio of light converted to heat, generally between 5 and 7%; and  $t$  is the thickness of the slab-shaped material.

According to the above equation, the authors estimated the light pumping limit of a unit volume of input that the following slabs can withstand, as well as the actual input powers in the experiment (see Table 1): model IV neodymium glass slab and YAG slab that the authors used in the University of Maryland in the United States, as well as the neodymium glass slab that other research units employed in the United States.

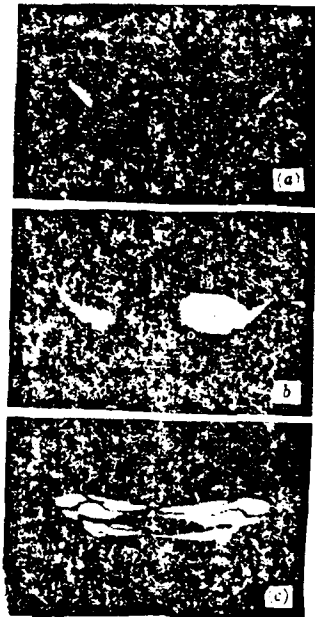


Fig. 9

KEY: (a) Stress diagram after installation of the fourth setup with face panel added (b) Stress diagram (face panel added) after water was connected to the setup (c) Stress diagram with light pumping input of 2645W, 5Hz

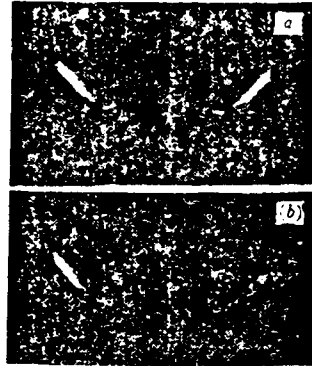


Fig. 10

Remark: (a) Stress diagram after installation of YAG (b) Stress diagram of YAG after cooling water was connected

TABLE 1

1 单位	2 材料	3 尺寸 (cm <sup>3</sup> )	4 理论极限值 (W/cm <sup>3</sup> )	5 实验输入值 (W/cm <sup>3</sup> )
马里兰大学 6	III型 Nd 玻璃 9	1.3×2.8×10	120	73
马里兰大学 6	YAG 10	1.3×2.8×10	780	158
光诺物理公司 7	Nd 玻璃 10	0.44×15×16.7	220	45
斯坦福大学 8	Nd 玻璃 10	0.63×5.6×35	440	21.5

KEY: 1 - Unit 2 - Material 3 - Dimensions (cm<sup>3</sup>)  
 4 - Theoretical limiting value (W/cm<sup>3</sup>) 5 - Input value in the experiment (W/cm<sup>3</sup>) 6 - University of Maryland 7 - Spectra Physics Corporation  
 8 - Stanford University 9 - Model III glass  
 10 - Nd glass

It can be seen that the phenomenon of glass without explosion cracking is a quite satisfactory experimental result

under stress-free installation conditions with the input of 2645W light pumping power (that is,  $73\text{W}/\text{cm}^3$ ) onto the authors' slab-shaped glass. If a similar method is used to install YAG, the light pumping power will greatly exceed  $158\text{W}/\text{cm}^3$  without leading to a break because the theoretical limiting value of YAG is much greater than that of Nd glass. Thus, it can be ensured that the YAG reflector lens type laser amplifier may achieve an output with a high energy, high repetition index.

The paper was received on 28 December 1987.

#### REFERENCES

1. Brown, David C., IEEE J. Quant. Electr. QE-17/9, 1755 (1981).
2. Koechner, W., Appl. Phys. (2), 279 (1973).
3. Narion, John E., VCRL-93 543.
4. Knske, A. et al., Photoelastic Stress Analysis, 103.
5. Huang Guosong et al., Jiguangbang Di Bengpu Gonglu Jixian [Limit of Laser Rod Pumping Power] (internal Chinese research circulating report).
6. Sasn, S. et al., Opt. Lett. (11), 1617 (1986).
7. Eggleston, J.M. et al., IEEE J. Quant. Electr. QE-22, 2092 (1986).

GAIN SATURATION PARAMETERS AND THEIR VARIATION IN  
TRANSVERSE-FLOW DISCHARGE CO<sub>2</sub> LASERS

Wu Zhongxiang, Institute of Mechanics, Chinese Academy  
of Sciences, Beijing

**Abstract:** By utilizing a combination method of numerical simulation computation and physical analysis, the algebraic equations of saturation gain and the gain saturation parameters of flowing-gas lasers are given; in addition, some factors and mechanisms affecting the equipment properties are qualitatively analyzed.

**Key technical terms:** numerical simulation, transverse flow, CO<sub>2</sub>.

## I. Introduction

The paper utilizes the numerical results obtained by simulation computation in [1] to analyze and compile the approximate algebraic equations suitable for the gas saturation coefficients of flowing-gas lasers; the equations also include the gain saturation parameter  $I_g$ . In addition, some factors affecting the saturation parameter are calculated and discussed, thus obtaining some rules that these saturation gain parameters vary with these factors. Moreover, some factors and mechanisms affecting the properties of these types of flowing-gas lasers are qualitatively analyzed. This method of deriving the algebraic

18 equations and important parameters by combining simulation computation and physical analysis is a new application of computational physics.

## II. Approximate Algebraic Equations of Gain Saturation Coefficients of Flowing-Gas Lasers

Under the given operating conditions in reference [1], from the simulation computational data showing that the small-signal gain  $G_0$  and the saturation gain vary with the corresponding light intensity  $I$  (these scans are at given positions in the optical cavity of transverse-flow discharge  $\text{CO}_2$  lasers), the corresponding constant  $I_S$  is selected. The quantities  $\lg G/G_0$  and  $\lg(1+I/I_S)$  are used, respectively, as the ordinate and abscissa to be plotted in Fig. 1.

In the calculation, the medium composition ratio is  $\text{CO}_2:\text{N}_2:\text{He}=5:17:78$ ; the height ( $h$ ) and length ( $L$ ) of the optical cavity are, respectively, 1.8cm and 160cm; the width ( $W$ ) along the gas flow direction of the optical cavity is 0.5cm; the distance ( $x_0$ ) is 0.1cm at the edge of the upper stream of the effective homogeneous zones departing from the edge of the upper stream; the electric field intensity ( $E/N$ ) of each particle is  $2.15 \times 10^{-16} \text{V}/\text{cm}^2$ ; the discharge current ( $J$ ) is 2 to 5A; the medium flow rate ( $u$ ) is 30 to 150m/s; and the gas pressure is 180 to 1200Torr at the fringe of the upper stream of the effective homogeneous discharge zone. The effective width of the homogeneous discharge zone linearly shortens with increase in gas pressure  $P$ ; this can be approximately expressed as:  
 $d(\text{cm}) \approx 1.172 - 0.000862P$  (Torr). The calculation point is at the position ( $x=0.1\text{cm}$  to  $0.6\text{cm}$ ; that is, the width of the optical cavity is 0.5cm) from the fringe in the upper stream of the optical cavity from the output lens surface of the optical cavity.

When  $I_S$  is appropriately selected and with all the conditions given above, the various points of  $\lg G/G_0$ ,  $\lg(1+I/I_S)$  (in Fig. 1) lie approximately on the same straight line. This indicates that the gain saturation coefficient can be approximately expressed (in these flowing-gas lasers with relatively high gas pressure) as follows:

$$G(P, u, I, x) \approx G_0(P, u, x) \times (1 + I/I_s(P, u, x))^{-r} \quad (1)$$

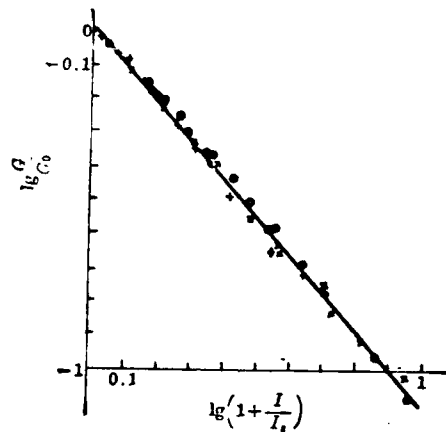


Fig. 1

●—200 Torr, ○—550 Torr, ×—780 Torr,  
+—1000 Torr,  $x=0.1\sim 0.6$  cm

In the equation,  $r \approx 1.11$ . This indicates a situation in which the decrease becomes more rapid with increase in light intensity for the saturation gain in flowing-gas lasers than in the case when the lasers do not have flowing gas because in a static situation,  $r=1$  (for the Lorentz-like pattern). Moreover, with the same  $I/I_S$ , more upper vibrational energy can be converted to laser energy; in addition, the gain saturation parameter  $I_S$  is a function of  $P$ ,  $u$ , and  $x$ .

### III. Some Factors and Variation Rules Affecting the Variation of Gain Saturation Parameters

Fig. 2 shows the variation curve of  $\lg I_s \sim x$  at a given flow rate and at several gas pressures; the solid lines and the dashed lines indicate, respectively, the variation within and without the corresponding homogeneous discharge zones. From the figure,  $\lg I_s$  decreases with increasing  $x$ . The rate of decrease is higher at the outset, but gradually diminishes with a continued increase in  $x$ . There is an apparent inflection point at the boundary between the solid and the dashed lines; this signifies that  $\lg I_s$  decreases more decidedly with variation in  $x$ .

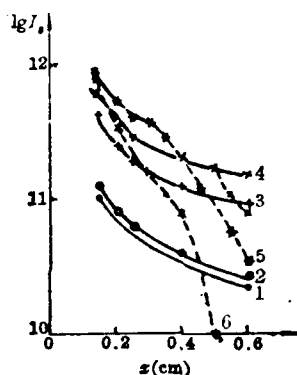


Fig. 2

1—180 Torr; 2—300 Torr; 3—550 Torr;  
4—780 Torr; 5—1000 Torr; 6—1200 Torr.

At inlet of optical cavity,  $x_0=0.1\text{cm}$ ;  
the medium flow rate  $u=30\text{m/s}$ ; for the  
solid lines,  $x < d$ ; for dashed lines,  
 $x > d$

Fig. 3 shows the curves in variation of  $\lg I_s \sim P$  at different positions under a given flow rate; the solid lines and the dashed lines also indicate, respectively, variation within and without the corresponding homogeneous discharge zones; from the figure,  $\lg I_s$  increases with increase in  $P$ ; the rate of increase is more rapid at the outset; however, the rate gradually slows down with a continual increase in  $P$ . There is also an apparent point of

inflection at the boundary between the solid line and the dashed line; this indicates that  $\lg I_S$  decreases more strongly with variation in  $P$  outside the effective homogeneous discharge zone.

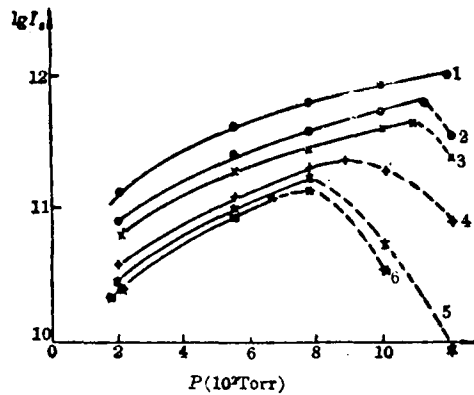


Fig. 3

1— $x=0.15$  cm; 2— $x=0.20$  cm; 3— $x=0.25$  cm;  
4— $x=0.40$  cm; 5— $x=0.50$  cm; 6— $x=0.60$  cm.

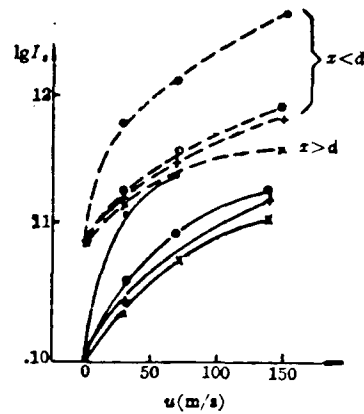


Fig. 4

●—0.15 cm; ○—0.40 cm; +—0.50 cm;  
×—0.60 cm, —200 Torr, .....780 Torr

$u=30$  m/s; for solid lines,  
 $x < d$ ; for dashed lines,  $x > d$

Fig. 4 shows the curves of variation of  $\lg I_S \sim u$  at different positions under two given gas pressures. From the figure,  $\lg I_S$  increases with increase in  $u$ . The rate of increase is steeper at the beginning; however, the rate gradually declines with the continued increase in  $u$ . By comparing the various dashed lines with gas pressure at 780 Torr, it also can be seen that  $\lg I_S$  decreases appreciably with variation of  $u$  after the examined points are outside of the homogeneous discharge zone (when  $P$  is approximately 780 Torr, the width is 0.5 cm for the effective homogeneous discharge zone). When  $u \rightarrow 0$ , at different positions  $I_S$  approaches the same value; however, the asymptotic values are different for different gas pressures. This indicates that  $I_S$  is not related to  $x$  for gas (not flowing) lasers; however,  $I_S$  is still a function of  $P$ .

Fig. 5 shows the curves of variation as  $\lg I_s \sim J$  at different positions with a given gas pressure and a given condition of flow rate. From the figure,  $\lg I_s$  basically remains constant with variation in the discharge current  $J$ .

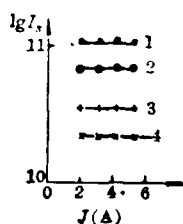


Fig. 5

●— $x=0.15$  cm; ○— $x=0.20$  cm; +— $x=0.40$  cm;  
 ×— $x=0.60$  cm,  $P=180$  Torr,  $u=30$  m/s

#### IV. Variation Mechanism of Gain Saturation Parameters

Under a given set of operating conditions and at a given position in the flowing-gas laser cavity, the variation of gain saturation with change in light intensity is exhibited by the particle population numbers of the medium between the upper and lower energy levels in the laser; the variation rule is expressed by Eq. (1), approximately.

Under the given steady fluctuation in light intensity, the larger the gain saturation parameter, the smaller is the saturation of the gain, and the larger is the relative difference in particle population numbers between the upper and lower laser energy levels of the medium.

In a discharged laser cavity, the difference of particle population numbers between the upper and lower laser energy levels will increase under the action of the electric pump; however, the action of the electric pump gradually tends to reach

saturation with increase in the residence time of the medium in the discharge zone. The greater the distance that the medium flows past in the discharge zone with a given flow rate, or the smaller the given flow rate of the medium at a given position in the discharge zone, the longer the residence time of the medium in the discharge zone, and the more saturated is the action of the electric pump. The difference of the particle population numbers between the upper and lower laser energy levels decreases under the influence of the following processes: spontaneous transitions, radiation-induced transitions, and collision relaxation, among other processes. Among these processes, the influence of radiation-induced transitions is apparently greater than that of spontaneous transitions. The effect of the electric pump and collision relaxation on the relative differences of the particle population numbers between the upper and lower laser energy levels grows stronger with an increase in gas pressure; among these processes, the effect of the electric pump tends to saturation because of a continuous increase in gas pressure. The addition of the effect of radiation-induced transitions caused by the medium flowing into the optical cavity and the appearance of the effect of the electric pump because of the medium flowing out of the discharge zone will cause the apparent decrease in the relative differences of the population numbers between the upper and lower laser energy levels. Increasing the discharge current can intensify the effect of pumping on the various laser energy levels; however, the upper and lower laser energy states increase at the same ratio, and basically do not change with change in the steady fluctuation of light intensity in the cavity.

The paper was received on 22 November 1987.

#### REFERENCES

1. Wu Zhongxiang, "Energy conversion properties and mechanism of transverse-flow discharge CO<sub>2</sub> lasers," Second All-China Computational Physics Conference, 1987, p. 9, Dayong, Hunan.

INFLUENCE OF ELECTRODE MATERIAL ON OPERATING LIFE  
OF LINE-SELECTION CO-CO<sub>2</sub> COMPOUND LASERS

Gui Zhenxing, Zhang Shunyi, and Shen Guirong, Shanghai Institute  
of Optics and Fine Mechanics, Chinese Academy of Sciences,  
Shanghai

Abstract: The authors experimentally studied the effect of  
electrode material on the operating life of line-selection CO-CO<sub>2</sub>  
compound lasers. As shown by the results, gold is more suitable  
as electrode material.

Key technical terms: gold, compound lasers, and line  
selection.

The authors reported on the operating properties [1] of  
line-selection CO-CO<sub>2</sub> compound lasers. This paper will further  
present the effect of electrode material on laser operating life.

There have been numerous reports on cathode materials for  
sealing type CO or CO<sub>2</sub> lasers [2-4]. However, these cathode  
materials may not be suitable for use in CO-CO<sub>2</sub> compound lasers  
because these lasers are filled with five gases: CO-CO<sub>2</sub>-N<sub>2</sub>-Xe-He,  
in addition to maintaining long-term stabilization of output  
power of CO or CO<sub>2</sub> lasers. By utilizing experience of earlier  
researchers, the authors conducted operating-life experiments on  
four materials: silver-copper, platinum, stainless steel, and  
gold.

As indicated by the results, gold is most suitable as electrode material.

Refer to [1] for a description of the laser used in the experiments; the anode of the discharge tube is a gold column with OD4mm; the cathode applies a cup-shaped structure with the internal surface area of the cylinder approximately 60 to 80cm<sup>2</sup>, with less sputtering. After the cathode was changed, vacuum baking treatment was conducted on the discharge tube in order to expel the miscellaneous gases that were adsorbed. The purity of all working gases used was higher than 99.9%. The output power was measured with a model SD2490 wattmeter. A high-voltage electrometer was used to monitor the variation of the discharge tube voltage; to eliminate the influence of the photocurrent effect, all the voltages measured in the experiment were potential drops at the discharge tube when the laser was not oscillatory; to a certain extent, the measured voltage exhibited the variation of gas composition in the discharge tube.

As indicated in the experiment, the intensity and the range of the output power spectrum underwent changes with continued operation of the device; under general conditions, the weaker the distribution of the spectral-line intensities, the lower the output of the spectral zone. Therefore, the paper selected the

$\left\{ \begin{array}{l} P_{10-0}(22) \\ P_{11-10}(16) \end{array} \right.$  (5.4micrometer) line of CO, and the 010P(20) (10.59micrometer) line of the 00<sup>0</sup>1-10<sup>0</sup> transition of CO<sub>2</sub>, to observe the variation in laser output power with time when different electrode materials were used.

As shown in Fig. 1, the output of CO was relatively stable, when a silver-copper anode (containing 95% silver and 5% copper) was selected. However, CO<sub>2</sub> spectral-line intensities dropped relatively rapidly. By adopting a platinum anode, the CO<sub>2</sub> spectral-line intensities increased with discharge time, but

decreased for CO (Fig. 2). Only the gold electrode fundamentally maintained the initial values of the CO and CO<sub>2</sub> spectral-line intensities after the device was continuously operated for 1000h (Fig. 3), although the output from CO exhibited a rise-and-fall type fluctuation. The worse case was found for the stainless steel anode, which lowered the output from CO and CO<sub>2</sub> relatively rapidly (Fig. 4). It can be found from Figs. 1 to 4 that the variation of the potential drop of the discharge tube basically corresponds to variation in spectral-line intensities of CO<sub>2</sub>. From [1], the intensities of CO and CO<sub>2</sub> lasers at the output from the laser device are closely related to CO<sub>2</sub> concentration. Therefore, variation in the pressure drop of the discharge tube also indirectly reflects the variation of CO<sub>2</sub> concentration in the gas.

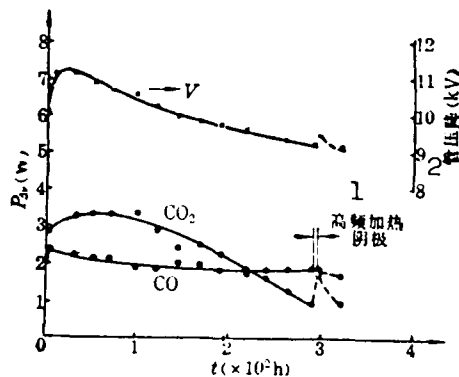


Fig. 1  
Silver-copper anode:

CO:CO<sub>2</sub>:N<sub>2</sub>:Xe:He=1:0.07:2:1.6:16

KEY: 1 - High-frequency heating anode 2 - Potential anode (kV) of the discharge tube

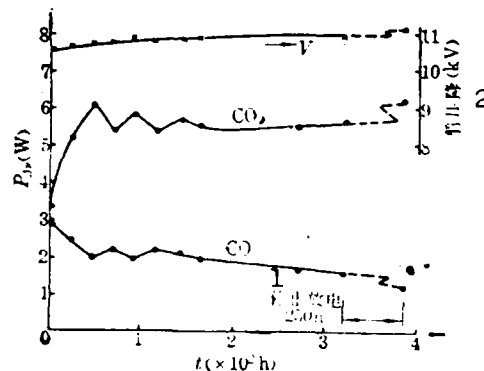


Fig. 2  
Remark: Platinum anode:

CO:CO<sub>2</sub>:N<sub>2</sub>:Xe:He=  
1:0.06:2:1.6:15.5

KEY: 1 - Suspension of discharge 2 - Potential drop (kV) of the discharge tube

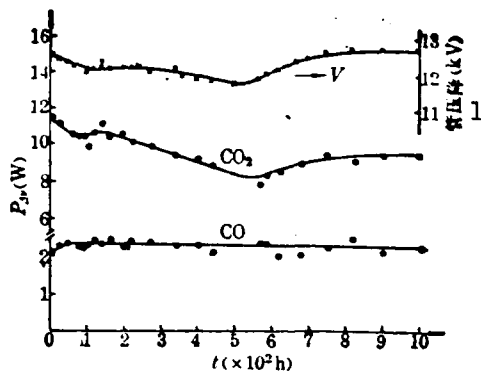


Fig. 3

Remark: gold anode:

$CO:CO_2:N_2:Ne:He=1:0.23:2:1.5:14$

KEY: 1 - Potential drop (kV) of discharge tube

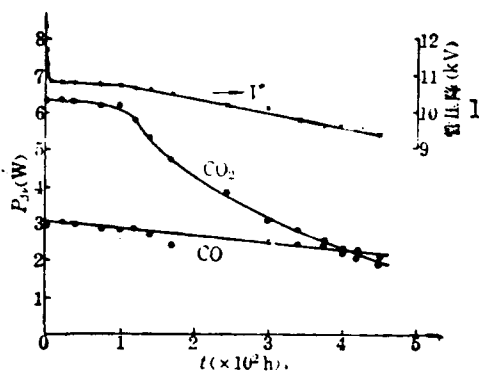


Fig. 4

Remark: stainless steel anode:

$CO:CO_2:N_2:Ne:He=1:0.27:2.2:1.45:15$

KEY: 1 - Potential drop (kV) of discharge tube

The above-mentioned results are due to variation in gas composition as well as variation of the content of CO and  $CO_2$  in the chemical reaction and the electrochemical process of gas and electrode in the discharge. As discovered in the authors' experiments, after prolonged discharge a black product appeared on the surface of the silver-copper anode; the product was assumed to be silver oxide produced by dissolving some of the  $CO_2$ . However, the platinum anode has a catalytic reducing effect on  $CO_2$ , continuously increasing the  $CO_2$  concentration and decreasing the amount of CO. The gold electrode has relatively stable chemical properties, not easily oxidizable and unreactive toward CO or  $CO_2$ . However, in the discharge process the authors discovered that a milky-white sorptive substance appeared on the tube wall near the anode; the substance became denser with time,

then gradually lightening. The process of variation basically corresponds to variation in the output power of the CO<sub>2</sub>. This substance is possibly a type of oxide of nitrogen; (electric) discharging with pure CO gas can remove the substance.

It can be seen that the key to maintaining stable power from CO and CO<sub>2</sub> lasers is control of the constant concentrations of CO and CO<sub>2</sub> in the mixed gas, especially the amount of CO<sub>2</sub>. Because in a compound laser an important means of excitation with CO<sub>2</sub> is VV collisions of low-oscillation state CO molecules, with an increase in CO<sub>2</sub> concentration, the number of high-oscillation-state CO particles should be lowered in order to lower the CO intensities. For the same reason, if the quantity of CO<sub>2</sub> is reduced, then this action is not expected to reduce the output power of CO<sub>2</sub>.

In the above discussion, no effect of other impurities is discussed. Actually, trace impurities of oxides of nitrogen and hydrocarbons, as produced in the discharge, also influence the operating life of the device. However, this is not the main factor in the overall experimental results.

The CO-CO<sub>2</sub> compound laser is basically a laser mainly relying on a CO laser medium and filling with small amounts of CO<sub>2</sub> gas. Therefore, this compound laser can be similarly adapted to technical processes for the development of long-operating-life sealed CO lasers. For example, highly purified gases to clean, bake, and vacuum degasify, among other operations [5], the discharge tube wall and electrodes. In addition, suitable electrode materials should be selected in order to reduce the dissolution and other chemical reactions of CO and CO<sub>2</sub>. As indicated by the results of this experiment, with the adoption of a gold electrode in CO-CO<sub>2</sub> compound lasers, higher output powers from CO and CO<sub>2</sub> lasers, as well as longer operating life, can be realized.

The paper was received on 21 December 1987.

#### REFERENCES

1. Gui Zhenxing et al., Guangxue Xuebao [Journal of Optics] 8/10, 911 (1988).
2. Browne, P. G. et al., Scient. Instr. 8/10, 870 (1975).
3. Hochul, U. E. et al., IEEE J. Quant. Electr. QE-10/2, 239 (1974).
4. He Guangsheng and Lei Shizhan, Jiguangqi Sheji Jichu [Laser Design Fundamentals], Shanghai Publishing House of Science and Technology, 1st ed., June, 1979, p. 166.
5. Zhang Shunyi et al., Jiguang [Lasers] 9/10, 643 (1982).

SPACE-VARIANT OPTICAL LOGIC OPERATION WITH  
 $\theta$ -MODULATION

Chen Henguang, Lu Wenpei, and Zhong An, Northwestern  
Polytechnical University, Xian

**Abstract:** The paper proposes a new method of optical logic operation in executing space variants; in other words, the various portions of space are conducted in parallel, different logic operations. By using the  $\theta$ -modulation technique, this method executes coding on the input binary variate and processes with the space filtration technique.

**Key technical terms:**  $\theta$ -modulation, logic operation, coding.

I. Implementation of Parallel Optical Logic Operations with  
the  $\theta$ -Modulation Technique

With the  $\theta$ -modulation technique, encoding is performed on the binary variate [1].

Assume that a gray-level graph is divided into N equal levels of gray. This can be expressed as follows:

$$I(x, y) = \sum_{n=1}^N (n/N) I_n(x, y)$$
$$I_n = 0 \text{ or } 1 \quad (1)$$

To accelerate the rate of coding, in general an optoelectronic

mixing method was adopted. The plot was recorded with a television camera to be inputted into a selector. Graphs of different gray levels were selected for display on a television monitor; a rotatable grating was placed in front of the camera to modulate a graph of a certain grayness.

The logic variate can be expressed in terms of a binary variate. In optics, black (opaqueness) represents 0 and white (transparentness) represents 1. With the  $\theta$ -modulation technique, 0 and 1 were modulated by using a pair of orthogonal gratings for coding (Fig. 1).

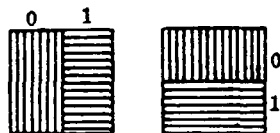


Fig. 1. Coding principle of  $\theta$ -modulation

The logic operation performed on two binary variates A and B can be listed with a 2x2 table of real-valued functions. Table 1 shows the relationship between all the 16 basic logic operations and the real-valued functions.

The optical system of implementing the logic operation was a series of two 4f systems, which are also called an 8f system (Fig. 2). Different filters were placed, respectively, on two filtration systems; thus, parallel logic operations can be performed. The filter on the first filtration system served in filtering the grating structure in order to avoid the formation of Moll streaks on the second input surface. The composition of the frequency spectrum on the first filtration is as follows:

$$0, \pm v_0, \pm v_1$$

A pinhole filter was placed on the first filtration surface so

that only  $v_0$  and  $v_1$  could pass through the pinhole. Then the frequency spectrum distribution on the second filtration surface was as follows:

$$v_0, v_1, v_0 \pm v_0, v_0 \pm v_1, v_1 \pm v_0, v_1 \pm v_1$$

Among these quantities,  $v_0$  and  $v_1$  are nondiffraction items, and  $v_0 - v_0$ ,  $v_1 - v_1$ , as well as  $v_0 + v_1$  and  $v_1 + v_0$  are overlapping items. The relationship between the frequency spectrum distribution and the real-valued function is as follows:

$$\begin{cases} I_{00} \Leftrightarrow v_0 + v_0 \\ I_{01} \Leftrightarrow v_0 - v_1 \\ I_{10} \Leftrightarrow v_1 - v_0 \\ I_{11} \Leftrightarrow v_1 + v_1 \end{cases}$$

On the second filtration surface, appropriate filters were selected, thus obtaining the required operational form.

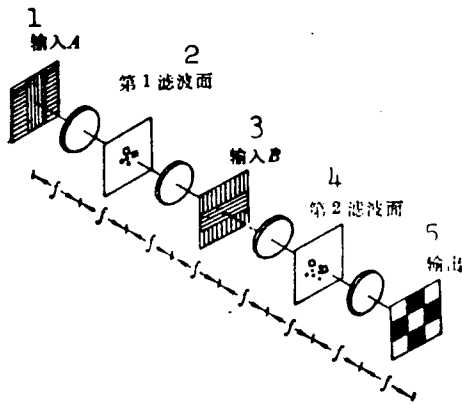


Fig. 2. Schematic diagram of 8f system (square-frame on the filtration surface indicates pinhole)  
 KEY: 1 - Input A 2 - First filtration surface 3 - Input B  
 4 - Second filtration surface 5 - Output

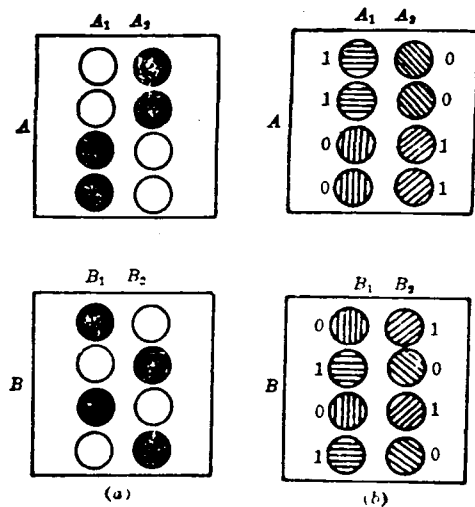


Fig. 3. Principle of multi-channel coding  
 Remark: (a) - Original graph (b) - Coded graph

## II. Optical Logic Operation of Space Variant

Assume two binary variates A and B are, respectively, divided into  $A_1$  and  $A_2$  as well as  $B_1$  and  $B_2$  (Fig. 3). It is required that two operations are simultaneously processed on the two corresponding parts.

$$\begin{cases} A_1 \text{ AND } B_1, \\ A_2 \text{ XOR } B_2. \end{cases}$$

After improvement, the coding mode is as shown in Fig. 3 (b). To  $A_1$  and  $B_1$ , as well as  $A_2$  and  $B_2$ , a pair of orthogonal gratings was used for coding. Here the gratings for coding  $A_2$  and  $B_2$  can be considered as the gratings for coding  $A_1$  and  $B_1$  by rotating  $45^\circ$  in the counterclockwise direction. The optical system of implementing the optical operation is still an 8f system; but now the frequency spectrum on the first and second filtration surfaces is more complex than the original spectral component on the first filtration surface as shown below:

$$0, \pm v_{10}, \pm v_{11}, \pm v_{20}, \pm v_{21}$$

Design the first filter by only letting  $v_{10}$ ,  $v_{11}$ ,  $v_{20}$ , and  $v_{21}$  to pass and filter the other frequency spectra; thus, we can avoid the Moll streaks appearing in the second input surface. The frequency spectral distribution on the second filtration surface is as follows:

$$\begin{aligned} &v_{10}, v_{11}, v_{10} \pm v_{10}, v_{10} \pm v_{11}, v_{11} \pm v_{10}, v_{11} \pm v_{11} \\ &v_{20}, v_{21}, v_{20} \pm v_{20}, v_{20} \pm v_{21}, v_{21} \pm v_{20}, v_{21} \pm v_{21} \end{aligned}$$

Among these quantities,  $v_{10}$ ,  $v_{11}$ ,  $v_{20}$ , and  $v_{21}$  are the nondiffraction items; and

$$\begin{aligned} &v_{10} + v_{11}, v_{11} + v_{20} + v_{21}, v_{21} + v_{20}; v_{10} - v_{10}, v_{20} - v_{20}, v_{11} - v_{11}, \\ &v_{21} - v_{21} \end{aligned}$$

are the overlapping items. The corresponding relation between the frequency spectrum and the real-valued function:

$$\begin{cases} I_{00}^* \Leftrightarrow v_{10} + v_{10} & I_{20}^* \Leftrightarrow v_{20} + v_{20} \\ I_{01}^* \Leftrightarrow v_{01} - v_{11} & I_{21}^* \Leftrightarrow v_{20} - v_{21} \\ I_{10}^* \Leftrightarrow v_{11} - v_{10} & I_{22}^* \Leftrightarrow v_{21} - v_{20} \\ I_{11}^* \Leftrightarrow v_{11} + v_{11} & I_{23}^* \Leftrightarrow v_{21} + v_{21} \end{cases}$$

TABLE 1. Logic Real Values Corresponding to 16 Types of Fundamental Logic Operations

1 真值变量	2 运算															
	0	$A \cdot B$	$A \cdot \bar{B}$	$A$	$\bar{A} \cdot B$	$B$	$A \oplus B$	$\overline{A+B}$	$\overline{A \cdot B}$	$\bar{B}$	$A+B$	$\bar{A}$	$\bar{A}+B$	$\overline{A \cdot B}$	$A+B$	1
$I_{00}$	0	0	0	0	0	0	0	1	1	1	1	1	0	1	0	1
$I_{10}$	0	0	1	1	0	0	1	0	0	1	1	0	0	1	1	1
$I_{01}$	0	0	0	0	1	1	1	0	0	0	0	1	1	1	1	1
$I_{11}$	0	1	0	1	0	1	0	0	1	0	1	0	0	0	1	1

KEY: 1 - Real-valued variate 2 - Operation

The corresponding values of the real-valued function with the operation on two corresponding parts in space are as follows:

$$A_1 \text{ AND } B_1 \leftrightarrow \begin{cases} I_{11} = 1 \\ \text{the remainder is 0.} \end{cases}$$

$$A_2 \text{ XOR } B_2 \leftrightarrow \begin{cases} I_{01} - I_{10} = 1 \\ \text{the remainder is 0.} \end{cases}$$

Therefore, the filter on the second filtration surface should be three pinholes letting through only  $v_{11} + v_{11}$ ,  $v_{20} - v_{21}$ , and  $v_{21} - v_{20}$ .

Fig. 4 is a set of experimental pictures showing the frequency spectrum and the results of the optical logic operation with space variant.

For a more general situation, A and B are separately divided into N portions  $A_i$  and  $B_i$  ( $i = 1, \dots, N$ ) for conducting different logic operations between the various corresponding parts, marked as follows:

$$A_i \{L_i\} B_i, i=1 \dots N.$$

From the special case, previously, when  $N=2$ , the coding specifications of  $A_i$  and  $B_i$  are as follows:

1. The coding diagram of  $A_1$  and  $B_1$  is as shown in Fig. 1;

2. The coding gratings of  $A_i$  and  $B_i$  are the coding gratings of  $A_1$  and  $B_1$  by rotating by an angle  $\theta_i$  in the counterclockwise direction; and

3. 
$$\theta_i = (i-1) \frac{\pi}{2N}.$$

The optical path of the optical logic operation of carrying out the space variant is still an 8f system. Now the frequency spectrum distribution is the first filtration surface:  $0, \pm v_{i0}, \pm v_{i1}$ , while  $i=1, \dots, N$ . The filter on the first filtration surface is  $n$  pinholes allowing  $v_{i0}, v_{i1}$  ( $i=1, \dots, N$ ) to pass through. Thus, the frequency spectrum on the second filtration surface is as follows:

$$\begin{aligned} &v_{i0}, v_{i1}, v_{i0} \pm v_{i0}, v_{i0} \pm v_{i1}, v_{i1} \pm v_{i0}, \\ &v_{i1} \pm v_{i1} \quad (i=1 \dots N) \end{aligned}$$

Now the corresponding relation between the real-valued function and the frequency spectrum is as follows:

$$\begin{aligned} I_{00} &\Leftrightarrow v_{i0} + v_{i0} \\ I_{01} &\Leftrightarrow v_{i0} - v_{i1} \\ I_{10} &\Leftrightarrow v_{i1} - v_{i0} \\ I_{11} &\Leftrightarrow v_{i1} + v_{i1} \end{aligned} \quad (i=1 \dots N)$$

From specifications about coding as mentioned above,  $v_i$  is obtained from  $v_1$  by rotating by an angle  $\theta_i$ . Therefore, the position of the frequency spectrum corresponding to  $I$  can be determined. Thus, performing the corresponding logic operation

on the various corresponding parts in space involves placing a definite number of pinholes so that the frequency spectra corresponding to  $M=1$ , as required by the operation may pass through.

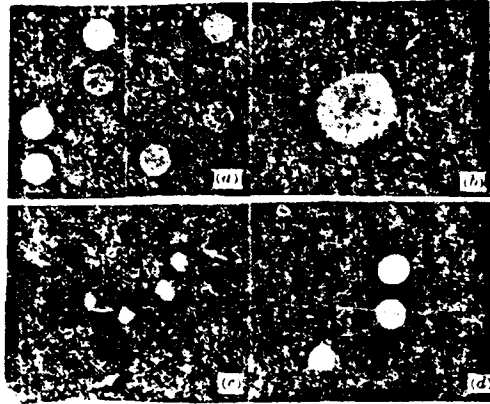


Fig. 4. Examples of optical logic computation and experiments with space variant; the examples are processed in parallel, AND and XOB operations  
Remark: (a) - Original picture of binary variate  
(b) First filtration surface (c) - Second filtration surface (d) - Experimental results

#### IV. Conclusions

As proposed in the paper, the coding method can have greater flexibility in optical operations. However, consideration should be given to the resolving power of the gratings when conducting multichannel coding; otherwise, there is the possibility of overlapping of various frequency spectra. By coding an optoelectronic mixing system, the coding grating of more than 100 line pairs can be obtained. Therefore, with the adoption of the ordinary He-Ne laser as the light source, no overlapping will occur between frequency spectra. Besides its use in optical logic computation of the space variant, this type of coding can also be applied in optical digital computation. However, coding should be carried out in advance of the input signals; however,

considering that a large quantity of information can be obtained at the output with parallel operations, this method can still be considered for use.

The authors are grateful to teachers in the physics laboratory in the Northwest Polytechnic University for their enthusiastic assistance. The authors express their sincere gratitude.

The paper was received on 9 November 1987.

#### REFERENCES

1. Bartelt, H. et al., Appl. Opt. 22, 2519 (1983).

## XeCl-LASER-INDUCED OXIDATION REACTION OF CERIUM SEPARATION

Zhou Zhenghuo and Qiu Mingxin, Shanghai Institute of Laser Technology, Shanghai; and Huang Shaitang, Bu Qixiu, Gu Jialiang, Li Fangling, and Shi Jiliang, Shanghai Institute of Organic Chemistry, Chinese Academy of Sciences, Shanghai

**Abstract:** The paper studies the use of a 308nm XeCl excimer laser to induce cerium separation with an oxidation reaction; the relative value of X-ray fluorescence spectrum to quantitative calibration, and the separation rates of cerium at different solvent parameters were obtained. The separation coefficient  $\beta=5.6$  was obtained in the blending solution of cerium and lanthanum.

**Key technical terms:** laser-induced, cerium, separation rate.

### I. Introduction

Lasers open a new, wide realm in optical chemistry; lasers are applied in various fields in laser chemistry, such as the study of laser chemistry dynamics, isotopic separation, and chemical purification, as well as laser-induced chemical reaction. The paper studies the separation oxidation-reduction reaction for the rare-earth element cerium; X-ray fluorescence spectra are used for quantitative analysis. When the element cerium in its liquid phase was exposed to a 308nm laser, the optically induced separation reaction with cerium is much more

significant than with the other lanthanide series elements. This is because of the 4f-5d electronic transition with energy corresponding to the energy of the 308nm XeCl excimer photons. The method of laser-induction oxidation-reduction chemical reactions is also adaptable to the other similar isotopic separations, including the treatment of waste nuclear materials; therefore, the method has a certain value.

Generally, there are two methods of deposition and extraction [1] for laser oxidation or reduction separation of elements. Products from the optical chemistry deposition methods are homogeneous with high purity; in addition, the process can be easily controlled and analyzed. The cerium oxidation reaction reported in the paper is the Ce produced chemical deposition through optical chemical means, thus making it possible to separate cerium from mixtures of the other rare-earth elements.

## II. Experimental Results and Analyses

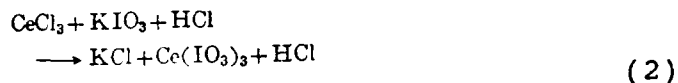
By the use of water-soluble ions of trivalent Ce, the following optical oxidation reaction can occur upon exposure to an ultraviolet source:



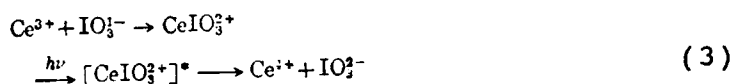
Here, the ultraviolet rays first excite the complexes of the ground state of trivalent cerium ions and water from the 4f to 5d energy bands; the 5d electrons dissociate further to oxidize, forming the tetravalent ions.

However, in the reaction equation (1) since  $[\text{Ce}^{2+}(\text{H}_2\text{O})]^*$  will very rapidly acquire quenching excited energy by collision with surrounding molecules, and at the same time the  $\text{Ce}^{4+}$  that is generated will also disappear due to reduction by the H free radicals, thus the  $\text{Ce}^{3+}$  trivalent ions will still be restored.

Therefore, the optical oxidation reaction should proceed in the  $\text{KIO}_3$  acid solution to produce  $\text{Ce}(\text{IO}_3)_4$  in order to greatly increase the yield rate of oxidation. The reaction process is shown in Eqs. (2), (3), and (4).



$\text{Ce}(\text{IO}_3)_3$  is highly soluble; in acidic solutions, Ce ions form complexes with iodate radicals:



Ultraviolet photons excite this complex chemical, and then, as shown in Eq. (1),  $\text{Ce}^{3+}$  is oxidized to  $\text{Ce}^{4+}$ :



In the experiments, the output of the XeCl excimer laser is in the range between 40 and 80mJ. The repetition rate is twice a second after the output beam converges by passing through a convex lens  $L_1$  ( $F_1=65\text{cm}$ ) and a cylindrical-surface lens  $L_2$  ( $F_2=4.5\text{cm}$ ), the light beam enters the solution after passing through the quartz window of the reaction pool. By adjusting the relative positions of the two lenses and the specimen pool, the energy density of the laser light can be changed from  $0.1\text{J}/\text{cm}^2$  to  $1.5\text{J}/\text{cm}^2$ . The luminosity of the laser in each experiment was in the range tens to hundreds of J; 2ml of solution was contained in the reaction pool. Since this paper mainly reports on research in the optically-induced oxidation reaction of cerium, most experiments did not use mixtures of rare earths in solution, but only cerium chloride  $\text{CeCl}_3$  in order to reduce the analytical errors of XFS. For better homogeneity of the solution in the

reaction process, blending was conducted by stirring by blowing nitrogen gas into the solution.

Since deposits were obtained after the solution sample was exposed to light, and the quantity of the deposits was limited, filter paper was used in the collection.

Fig. 1 shows the relative rate of deposition of cerium at different concentrations of  $\text{KIO}_3$ . The relative rate of deposition is the amount deposited divided by the number of pulses and the laser energy in each pulse; in other words, this is the amount deposited per unit energy at 308nm.

With increase in the concentration of  $\text{IO}_3^-$  in the solution, the reaction continuously proceeded in the direction of stronger oxidation of  $\text{Ce}^{3+}$  and weaker reduction of  $\text{Ce}^{4+}$ , to arrive at a new equilibrium state in optical chemistry to deposit more Ce. The authors know that the oxidation potential energy of the ground state  $\text{Ce}^{3+}$  in  $\text{HCl}$  solution is  $E_0 = -1.28\text{eV}$ . But when  $\text{IO}_3^-$  was used as the oxidizing agent with  $E_0 = +1.1\text{eV}$ , this was not enough to oxidize  $\text{Ce}^{3+}$ . However, as in Eq. (3),  $\text{IO}_3^-$  can oxidize  $\text{Ce}^{3+*}$  for the excitation energy band from 4f to 5d, in achieving the purpose of separation. After the  $\text{KIO}_3$  concentration was higher than  $0.2\text{M/L}$ , a saturation trend appeared; this was possibly related to the constant concentration of  $\text{Ce}^{3+}$ . By holding the  $\text{HCl}$  and  $\text{KIO}_3$  concentrations in the solution constant, the curve plotted in Fig. 2 shows the relation between the rate of cerium deposition versus different  $\text{CeCl}_3$  concentrations. From Eqs. (2) and (3), in the solution the trivalent Ce ions formed complexes with the  $\text{IO}_3^-$  radicals; after excitation with the ultraviolet photons, the trivalent Ce ions were again oxidized by  $\text{IO}_3^-$  to tetravalent ions. Therefore, only when there were enough  $\text{IO}_3^-$  in the solution to form complexes, did the amount of cerium that was separated become larger with increasing  $\text{CeCl}_3$  in the solution. This trend is fairly well pronounced in Fig. 2.

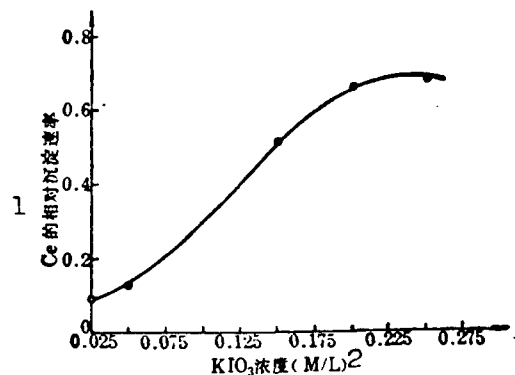


Fig. 1. Deposition rates of cerium at different  $\text{KIO}_3$  concentrations  
 Remark:  $\text{HCl}$ : 2M/L;  $\text{CeCl}_3$ : 0.02M/L  
 Solution: 2ml; laser dosage: 120J  
 KEY: 1 - Rate of Ce deposition 2 -  $\text{KIO}_3$  concentration (M/L)

With the same laser conditions and maintaining the same solution compounding ratio, the laser (at different power densities) strongly affects the yield rates (refer to Fig. 4). In the figure, the range in variation of laser power density is 0.1 and  $1.4\text{J}/\text{cm}^2$ ; with increase in power density, the amount of cerium deposited shows a decreasing trend. In the experiments, the authors changed the power densities by changing the focus of the laser spots; with increase in power densities, the irradiation region of the light pulses also becomes smaller. However, the value of the absorption peak of  $\text{Ce}^{3+}$  lies in the vicinity of 250nm, and then the absorption coefficient is  $720\text{M}^{-1}\cdot\text{cm}^{-1}$ . However, at 308nm of the XeCl laser, the absorption coefficient is only  $12\text{M}^{-1}\cdot\text{cm}^{-1}$ . Therefore, when the power density of the laser spots is too high, most of the laser energy is absorbed by the solution, raising the temperature and thus reducing the yield rate.

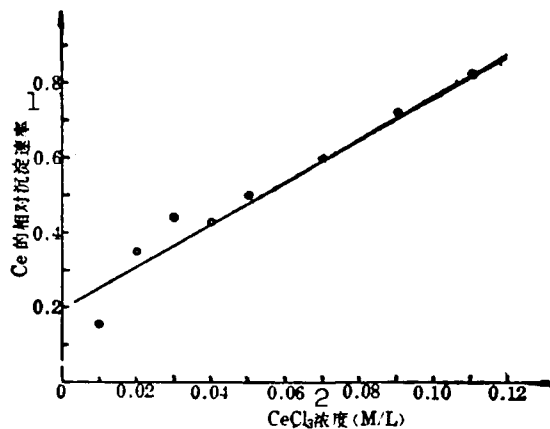


Fig. 2. Relative amounts of cerium deposited at different  $\text{CeCl}_3$  concentrations  
 Remark:  $\text{HCl}$ : 2M/L;  $\text{KIO}_3$ : 0.1M/L; solution: 2ml; laser dosage: 120J  
 KEY: 1 - Rate of Ce deposition 2 -  $\text{CeCl}_3$  concentration (M/L)

To observe the separation effect of the above-mentioned oxidation-reduction process in actual rare-earth mixtures, in experiments rare earth chlorides were used in replacing  $\text{CeCl}_3$  for laser irradiation; the solution used was 4.5ml; the compounding ratio was rare earth chloride  $\text{KIO}_3$ : $\text{HCl}$ =0.01:0.1:2. Both irradiation deposits were treated with the same method and measured with an XFS laser. Owing to difficulties in calibration of the instruments, only a rough comparison was made on two rare-earth elements (Ce and La binary constituents as the main constituents) in  $\text{LaCl}_3$  and  $\text{CeCl}_3$  in solution before separation, and in deposition after separation. As a result, an apparent separation effect with Ce can be observed. According to the definition of the separation factor  $\beta$ :

$$\beta = \frac{[\text{Ce/La}]_{\text{(沉淀)}}}{[\text{Ce/La}]_{\text{(起始)}}$$

[explanation of Chinese characters in the expression: numerator--deposition; denominator--beginning]

It can be calculated that the value of  $\beta$  is 5.6.

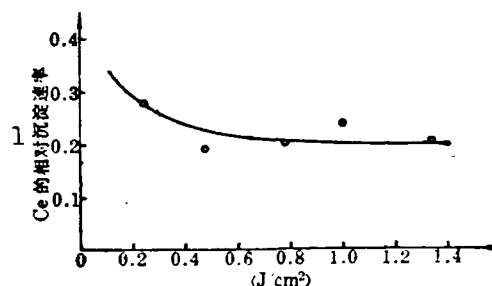
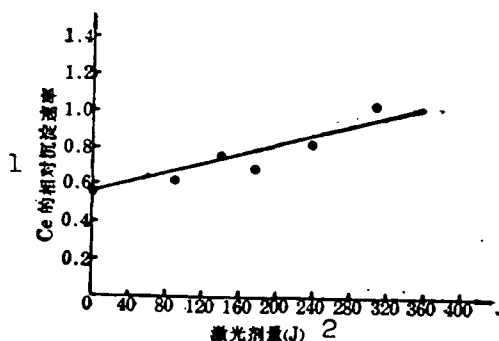


Fig. 3. Curve showing the cerium deposition rate when exposed to laser at different energies  
Remark:  $\text{CeCl}_3$ : 0.04M/L;  $\text{KIO}_3$ : 0.1M/L;  $\text{HCl}$ : 2M/L; solution: 2ml  
laser power density:  $0.53\text{J}/\text{cm}^2$ ;  
 $\text{CeCl}_3$ :  $\text{HCl}$ :  $\text{KIO}_3$  = k0.04:2:0.1  
KEY: 1 - Relative rate of Ce deposition 2 - Laser power (J)

Fig. 4. Effect of laser power densities on yield rate  
Remark:  $\text{CeCl}_3$ : 0.04M/L;  $\text{KIO}_3$ : 0.1M/L; solution: 2ml  
laser dosage: 122.7J  
KEY: 1 - Relative rate of Ce deposition

The paper was received on 4 January 1988.

#### REFERENCES

1. Donohue, Terence, Chem. Phys. Lett. **61**, 601 (1979).

RESONANCE FLUORESCENCE SHIFT IN Mg ATOMIC ISOTOPES WITH  
ULTRAVIOLET LASER

Wang Yuzhi,\* Shanghai Institute of Optics and Fine Mechanics,  
Chinese Academy of Sciences, Shanghai; N. Beverini and F.  
Strumia, Department of Physics, Pisa University, Italy

Abstract: Frequency standards are given with a Fabry-Perot interferometer. When magnesium atoms in an atomic particle beam were exposed to an ultraviolet laser beam acting perpendicular to the atomic particle beams, resonance fluorescence emission of magnesium atomic isotopes was generated. The resonance fluorescence shifts of magnesium atomic isotopes were measured for  $^{24}\text{Mg}$ ,  $^{25}\text{Mg}$ , and  $^{26}\text{Mg}$  at 285.2nm.

Key technical terms: Mg atoms and resonance fluorescence shift.

## I. Introduction

There have been numerous research studies on the magnesium isotopic shift at the resonance line  $\lambda=285.2\text{nm}$  [1-6]; however, the experimental results are quite varied. Relatively precise experimental results were given by Hallstadius [7-8]. In his experiments, the excited hollow cathode and the discharge tube were cooled with liquid nitrogen at the same time to produce

\*ICTP Fellow in Trieste, Italy

samples of magnesium atomic isotopes. By using the Fabry-Perot interferometer, frequency standards were recorded. Years later, there have been no similar reports. In this paper, when magnesium isotope atoms produced with the atomic beam furnace were exposed to a vertically incident ultraviolet resonance laser, fluorescence emission was produced. By using the Fabry-Perot interferometer, frequency standards were given. The experimental results are the same as those in reference [8].

## II. Experimental Setup

Fig. 1 shows a block diagram of the experimental setup.

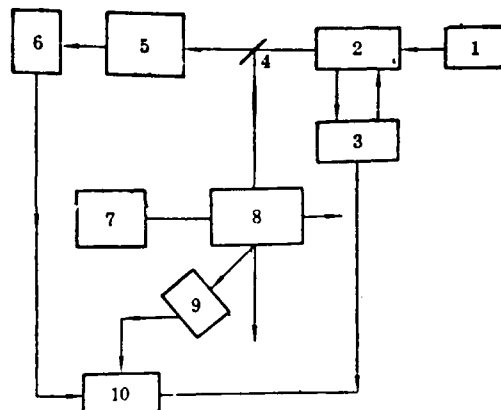


Fig. 1. Block diagram of experimental setup  
 Remark: 1 - Ar<sup>+</sup> laser 2 - No. 699 double-frequency dye laser 3 - Laser frequency control 4 - Beam splitter 5 - Fabry-Perot interferometer 6, 9 - Optoelectronic detectors 7 - Magnesium atomic beam furnace 8 - Atomic beam drift tube 10 - Recorder

The atomic beam furnace was 150mm in height, with three layers. The diameter of the outermost layer was 70mm; the furnace body temperature was 480°C; the temperature of the nozzle

was 488°C; and the abundance of the natural magnesium isotopes is as follows:  $Mg^{24}=78.70\%$ ;  $Mg^{25}=10.13\%$ ; and  $Mg^{26}=11.17\%$ . After the magnesium atomic beam produced in the furnace exited from the nozzle, the atomic beam entered in a drift tube in order to interact with the resonance laser, the beam of which was vertically incident.

By using a No. 699 ring-shaped dye laser (8W output) pumped with an  $Ar^+$  laser, the output at 570.4nm was 1.5W. Downstream of a double-frequency, internal-cavity type KDP crystal, a 285.2nm ultraviolet output was produced. The output at this wavelength acted on the magnesium atomic beam.

The Fabry-Perot interferometer is composed of two concave lenses (32cm in spacing between the two lenses) with the same radius of curvature. The radius of curvature was equal to the spacing between the two spherical-surface lenses; the focal length of the spherical-surface lens was 16cm. The distance between the optoelectronic detector and a reflector lens was 32cm. The cavity length was adjustable with a PZT.

### III. Experimental Results and Discussion

First, the frequency control system of the laser was adjusted to maintain a steady output of the No. 699 ring-shaped dye laser, which is a single-mode, 2MHz linewidth ultraviolet laser. The scanning frequency of the laser was 16GHz. Then resonance absorption was induced between the laser beam and the magnesium atomic beam; on a fluorescent screen of an oscilloscope, fluorescence transition at 285.2nm of magnesium was observed, as shown in Fig. 2.

From the figure, three apparent peaks can be observed; these peaks are caused by drift of magnesium atomic isotopes; now the Fabry-Perot interferometer was adjusted so that the coherence

condition  $\Delta l = m\lambda$  was satisfied. Fig. 3 shows the scanning plot displayed on the oscilloscope and received with an optoelectronic detector.

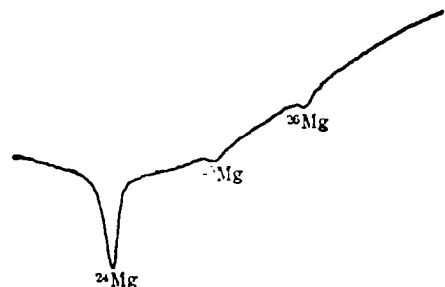


Fig. 2. Fluorescence emission of magnesium atomic isotopes:  $^{24}\text{Mg}$ ,  $^{25}\text{Mg}$ , and  $^{26}\text{Mg}$

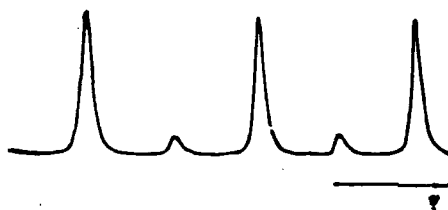


Fig. 3. Free optical spectrum scanning plot generated by the Fabry-Perot interferometer

Now the range of the free optical spectrum between the two peaks is  $1190.4 \pm 0.2\% \text{MHz}$ . When we compare Fig. 2 with Fig. 3, the isotopic drift of  $^{24}\text{Mg}$ ,  $^{25}\text{Mg}$ , and  $^{26}\text{Mg}$  can be measured.

The experimental results are listed in Table 1.

The authors' measurements are found to be consistent with the measurements obtained by Hallstadius; thus, the imprecise experimental results of the earlier research [1-6] can be corrected.

TABLE 1. Isotopic Drift of Mg 285.2nm Resonant Line

实 验 1	$^{25-24}\text{Mg}(\text{MHz})$	$^{26-24}\text{Mg}(\text{MHz})$
本 文 2	$743.2 \pm 10$	$1416.8 \pm 12$
Hallasadius	$728.5 \pm 12$	$1412.0 \pm 21$

KEY: 1 - Experiment 2 - This paper

The paper was received on 28 December 1987.

REFERENCES

1. Westmeyer, H., Z. Physik **94**, 590 (1935).
2. Jacksony, D. A. and H. G. Kuhn, Proc. Roy. Soc. A154, 679 (1936).
3. Fisher, R. A., Phys. Rev. **51**, 381 (1937).
4. Fisher, R. A., Rev. Mod. Phys. **14**, 79 (1942).
5. Murakawa, K., J. Phys. Soc. Japan **8**, 218 (1953).
6. Kelly, F. M., Can. J. Phys. **35**, 1320 (1957).
7. Hallstadius, Lars, Z. Physik A285 365 (1978).
8. Hallstadius, Lars, Z. Physik A291, 203 (1979).

## IDEAL SIZE OF LASER SPOT IN LASER PRINTING AND ITS MEASUREMENT

Li Qingxiong, Qian Qiuming, and Zhao Jianming, Shanghai Institute of Optics and Fine Mechanics, Chinese Academy of Sciences, Shanghai

**Abstract:** In laser printing, the ideal dimensions of laser spot are analyzed; the theoretical basis of design is given; a computerized measurement system is established.

**Key technical terms:** laser printing, optical scanning, optical transfer function.

### I. Foreword

Shortwave length semiconductor lasers are used as the light source in laser printers and laser typesetting machines; these machines underwent rapid development owing to their high quality output and low noise. The paper describes the use of optoelectronic scanning in measuring laser spot dimensions and the corresponding relation between the characteristic point on the optoelectronic scanning curve and laser spot dimensions. On this basis, a microcomputer-controlled optoelectronic scanning measurement system was constructed; by using a two-dimensional cutter blade, measurements can be made automatically along the scanning direction, thus providing the precise results of the entire line.

### II. Principles

Most present-day laser printers and laser phototypesetting machines use semiconductor lasers as their light source in emitting an astigmatic light beam with a divergence angle of about  $10^\circ$  in the direction of the parallel junction, and a divergence angle of  $30^\circ$  to  $40^\circ$  in the direction of the vertical junction. The light beam passes through an optical scanner to arrive at a photosensitive drum or photosensitive film, forming the image and the letter in the print-out as shown in Fig. 1.

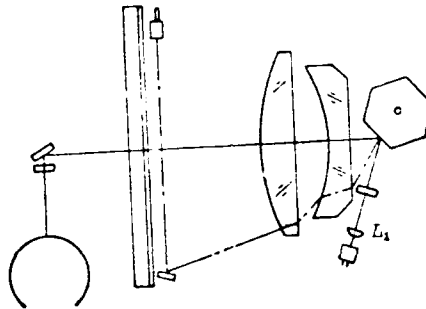


Fig. 1. Laser scanner

Coming from the semiconductor laser, a light beam with an elliptical cylindrical cross section first passes through a collimating lens  $L_1$  with  $F=2$ ; the laser beam will be interrupted to a differing extent. Therefore, the distribution of the image surface light beam is closer to the square of the Bessel function. However, the difference of laser spot shape is very small compared to the gaussian distribution. For sake of simplification, the discussion relies on the gaussian distribution.

From a focusing laser, the laser spot from the  $TEM_{00}$  mode

light beam can be expressed by the radius  $r_0$  of "1/e<sup>2</sup>":

$$I(r) = I(0) \exp[-2(r/r_0)^2] \quad (1)$$

In the equation,  $I(0)$  is the intensity at the center of the laser spot;  $r$  is the distance from the center; and  $r_0$  is the value of  $r$  when  $I(r) = I(0)/e^2$ . Generally, there is a radius  $r_1$  corresponding to the light intensity at the half-power point:

$$r_1 = 0.589 r_0 \quad (2)$$

the defined diameter of the laser spot is the full-width, half-maximum (FWHM) diameter, that is:

$$\text{FWHM} = 0.589 \omega_0 \quad (3)$$

In the equation,  $\omega_0$  is the beam waist;  $\omega_0 = 2r_0$ .

Laser scanning is intermittent in the direction the paper is moving; however, laser scanning is continuous in the direction vertical to the moving paper.

For the write system in laser printing, a certain distribution of the amount of light exposure is formed after laser scanning considering that the system MTF is determined by the bandwidth of FWHM and the modulator (its internal modulation for a semiconductor laser). In the following, the authors call the size of the image element (determined by the requirement of the resolving power) is  $D_r$ , which is the reciprocal of the resolving power.

Consideration is given to how the distribution of amount of light exposure at the optical detector is affected by the modulation bandwidth and the ratio between the FWHM and  $D_r$ . Fig. 2 is a diagram showing related parameters. The curve in the top figure represents an ideal object of spatial frequency; the middle figure shows the optical form emitted by the laser spot as the ascending time  $t_r$  is restricted by the bandwidths of the electronic circuit and the laser tube. If the effect of the driving electronic circuit is sufficiently rapid, the ascending time is determined solely by the laser tube proper and may attain

the nanosecond level. The curve in the bottom figure indicates the distribution of the amount of light exposure at the optical detector after scanning.

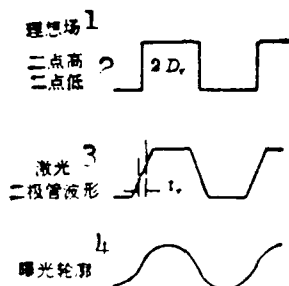


Fig. 2. Several related parameters  
 KEY: 1 - Ideal field 2 - Two points high and two points low 3 - Laser spot waveform 4 - Outline of light exposure

We can assume that the ascending time of the light waveform is equal to its descending time; that is,  $t_r = t_f$ . For a stationary scanning optical system, the point diffusion function is shown in Eq. (1). When scanning with a laser spot, the light point moves on the optical detector; the point diffusion function will expand. According to Eq. (1), the intensity distribution at the instant  $t$  is as follows:

$$I(x, y, t) = I(0) \exp[-2((x - vt)^2 + y^2)/r_0^2] \quad (4)$$

In the equation,  $v$  indicates the scanning rate. In addition, we can assume that the light waveform of the laser is time-domain-modulated by the following dimensionless function; this function corresponds to an object in space frequency (two points white and two points black):

$$i(t) = \begin{cases} [1 - \exp(-(t/t_r - 4N))] + [\exp(-2) \\ + \exp(-4)] & 4N < t/t_r < 4N+2 \\ [1 - \exp(-2)] \exp[t/t_r - (4N+2)] \\ & 4N+2 < t/t_r < 4N+4 \end{cases} \quad (5)$$

In the equation,  $N=1, 2, 3, \dots$ ; the amount of light exposure of a certain point  $(x, y)$  on the medium is recorded as:

$$E(x, y) = \int_0^{\infty} i(t) I(x, y, t) dt \quad (6)$$

consider the amount of light exposure on the line  $y=0$ , and substitute Eqs. (3), (4), and (5) in Eq. (6); moreover, by defining:

$$RA = \text{FWHM}/D_r \quad (7)$$

we find

$$E(x) = C \int_0^{\infty} i(t) \exp[-2(x-vt)^2 / (1.7RAD_r)^2] dt \quad (8)$$

In the equation,  $C$  is a constant factor; assume

$$D_r = Kvt_r \quad (9)$$

Insert Eq. (9) in Eq. (8); after normalization, we obtain:

$$E_N(x) = \int_0^{\infty} i(t) \exp[-0.69((x/D_r - t/Kt_r)/RA)^2] dt \quad (10)$$

Fig. 3 shows the curve of the normalized amount of light exposure versus  $X/D_r$  when  $K=1$  and  $RA$  is 1. Fig. 4 shows the curves of the amount of light exposure modulation versus  $RA$  when  $K=1, 4$ , and 7.

For a laser printing system, it is required only to obtain two-dimensional figures and letters; therefore, it is expected that the recording medium will have high contrast. This means that the slope of the  $H$  versus  $D$  of the film is very high when film is used; however, when a photoconductive drum is used, the curve of the attenuation of the surface electric potential versus the amount of light exposure is very steep.

In a laser printer, the curve of the printed figure density versus the logarithm of the amount of light exposure is very

steep. Therefore, when  $K=1$ , we can assume:

$$\text{FWHM(扫描方向)}=0.5 D, \quad (11)$$

[the Chinese characters in the parentheses in the above formula mean scanning direction]

When  $K=7$ , we assume:

$$\text{FWHM(扫描方向)}=0.9 D, \quad (12)$$

[explanation as given above for the Chinese characters]

In a laser phototypesetting machine, if it is required to attain 60% modulation (4:1 contrast) and if the slopes of the H versus D curves are 4, then when the logarithm of the amount of the light exposure is 0.6, the difference of output density can be 2.4. If we assume  $K=4$ , then we adopt:

$$\text{FWHM(扫描方向)}=0.4 D, \quad (13)$$

[explanation as given above for the Chinese characters]

If  $K=7$ , then we assume

$$\text{FWHM(扫描方向)}=0.7 D, \quad (14)$$

[explanation as given above for the Chinese characters]

The situation is much simpler in the direction of the moving paper. Vertical lines in the outputted figures and letters can be considered as the superpositioning of a series of stationary points. Emmel [1] presented a result concerning an object of one white and one black area. If FWHM is equal to the scanning line spacing, a modulation of 77% can be obtained. For laser printers, if we wish to achieve 50% modulation, we can assume:

$$\text{FWHM(走纸方向)}=1.23 D, \quad (15)$$

[Chinese characters in the parentheses above mean direction of moving paper]

For a laser typesetting machine, if the properties of the film used are the same as those mentioned above and if we intend to achieve 60% modulation, we can set FWHM as follows:

$$\text{FWHM(走纸方向)}=1.18 D, \quad (16)$$

[Chinese characters in the parentheses above mean direction of

moving paper]

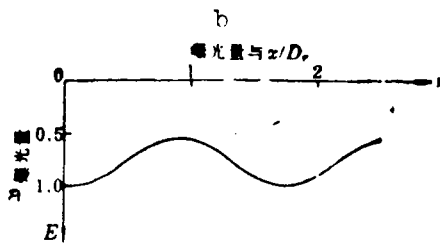


Fig. 3. Distribution of amount of light exposure and  $x/D_r$  curve  
 Remark:  $RA=1$ ;  
 modulation is 0.282465  
 KEY: a - Amount of light exposure b - Amount of light

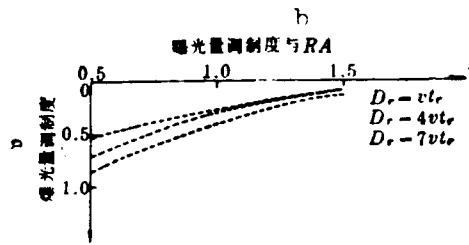


Fig. 4. Relation curves ( $K= 1, 4, \text{ and } 7$ ) of amount of light exposure modulation versus  $RA$   
 KEY: a - Amount of light exposure modulation b - Amount of light exposure and  $RA$

### III. Measurement of Laser Spot Size

The laser spot is measured with a photocell behind a cutter blade; the cutter blade is driven by a spider mechanism made of a piezoelectric ceramic, a product of the Burleigh Instrument Corporation in the United States. When the two-dimensional cutter blade scans, respectively, in the  $x$  and  $y$  directions, the curve of the photocell output versus displacement is obtained. Fig. 5 shows the optoelectronic portion of the measurement setup.

For the distribution of light intensity as shown in Eq. (1), the total energy measured by the authors is given by the following equations:

$$\Phi(x_0) = \int_{-\infty}^{\infty} \int_{-\infty}^{\infty} I(0) \exp(-2(x^2 + y^2)/r_0^2) dy \quad (17)$$

$$= 2I(0) \int_{-\infty}^{x_0} \exp(-2x^2/r_0^2) dx \quad (18)$$

$$\times \int_{-r_0}^{r_0} \exp(-2y^2/r_0^2) dy \quad (19)$$

$$= CI_0 [1 + \operatorname{erf}(\sqrt{2} x_0/r_0)]$$

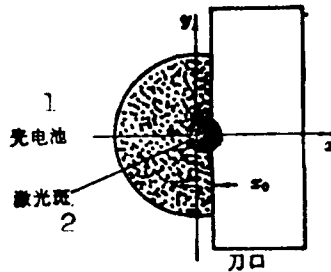


Fig. 5. Scanning cutter blade  
KEY: 1 - Photocell 2 - Laser spot

In the equations,  $C$  is a constant and  $\operatorname{erf}$  indicates the error function. When  $x_0$  tends to infinity,  $\phi(x_0)$  tends to  $\phi_{\max}$ ; by using  $\phi_{\max}$  to normalize  $\phi(x_0)$ , we obtain a normalization function  $\phi_N(x_0)$ :

$$\phi_N(x_0) = 0.5 [1 + \operatorname{erf}(\sqrt{2} x_0/r_0)] \quad (20)$$

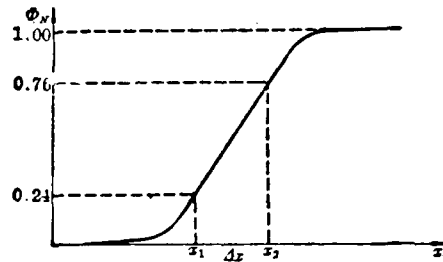


Fig. 6. Optoelectronic output curve

Fig. 6 indicates a curve obtained with this optoelectronic scanning. On the curve, the authors found the points  $x_1$  and  $x_2$  corresponding to 0.24 and 0.76  $\phi_N$ . By referring to the error function table, the authors obtained the following equations of the relation:

$$\begin{cases} x_1 = -0.35 r_0 \\ x_2 = +0.35 r_0 \\ \Delta x = 0.7 r_0 \end{cases} \quad (21)$$

Thus we can know precisely the " $1/e^2$ " radius and the FWHM:

$$\begin{aligned} r_0 &= 1.43 \Delta x \\ \text{FWHM} &= 1.67 \Delta x \end{aligned} \quad (22)$$

The purpose of taking 0.24 and 0.76  $\phi_N$  is to obtain the steeper parts of the curve, thus achieving higher precision. Fig. 7 is a diagram showing the measurement system. When the cutter blade (located on a "spider" work platform) moves, the electric signals coming from the photocell are fed into an x-y recorder and a microcomputer. Through an electric induction type micrometer, the displacement signal of the "spider" work platform is also fed to the recorder and the microcomputer. By analysis (manual or automatic) of the curve shown in Fig. 6, we can obtain the magnitude of FWHM.

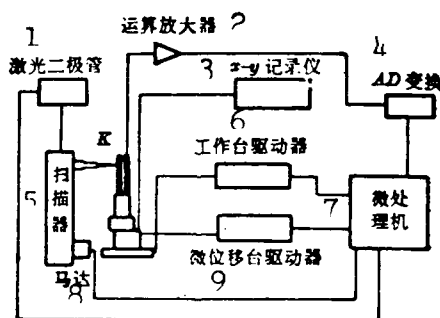


Fig. 7. Block diagram of the measurement system  
 KEY: 1 - Laser diode 2 - Computation amplifier  
 3 - x-y recorder 4 - AD conversion 5 - Scanner  
 6 - Driver at work platform 7 - Microprocessor  
 8 - Motor 9 - Driver at microdisplacement platform

The paper was received on 21 January 1988.

#### REFERENCES

1. Emmel, P. M., "Laser scanning and recording for advanced image and data handling," SPIE Proceedings, Vol. 222, p. 2 (1980).

DISTRIBUTION LIST

DISTRIBUTION DIRECT TO RECIPIENT

<u>ORGANIZATION</u>	<u>MICROFICHE</u>
C509 BALLISTIC RES LAB	1
C510 R&T LABS/AVEADCOM	1
C513 ARRADCOM	1
C535 AVRADCOM/TSARCOM	1
C539 TRASANA	1
Q591 FSTC	4
Q619 MSIC REDSTONE	1
Q008 NTIC	1
E053 HQ USAF/INET	1
E404 AEDC/DOF	1
E408 AFWL	1
E410 AD/IND	1
F429 SD/IND	1
P005 DOE/ISA/DDI	1
P050 CIA/OCR/ADD/SD	2
AFTT/LDE	1
NOIC/OIC-9	1
CCV	1
MIA/PHS	1
LLYL/CODE L-309	1
	1
NSA/T513/TDL	2
ASD/FTD/TITA	1
FSL	1